University of Stavanger

Faculty of Science and Technology

MASTER'S THESIS

Study program/ Specialization: MsC in Mathematics and Physics	Spring semester, 2016 Open
Writer: Matteo Busi	Matteo Busi
Faculty supervisor: Helge Bøvik Larsen External supervisor(s): David Graham Nicholson	
Thesis title: Self-Absorption Corrections in Fluorescence EXAFS	
Credits (ECTS): 60	
Key words: Physics, Mathematics X-Ray Physics	Pages: 65 + enclosure: 0 Stavanger, 15-06/2016 Date/year

Front page for master thesis
Faculty of Science and Technology
Decision made by the Dean October 30th 2009

Self-absorption corrections in Fluorescence EXAFS

Matteo Busi

June 2016

MASTER THESIS

Institutt for matematikk og naturvitskap

Universitet i Stavanger, Norway

Supervisor: Helge Bøvik Larsen

Preface

This is the Master Thesis final report of the research work carried through the 2015 Fall and 2016 Spring semesters to complete the Master Programme in Physics at the University of Stavanger. The subject of the research is within the X-Ray Physics, regarding experimental technique called EXAFS (Extended X-Ray Absorption Fine Structure) frequently used, for instance, in chemistry and biophysics measurments.

Stavanger, Norway. 15 June 2016

Matteo Busi

Acknowledgment

I must first of all thank my supervisor Helge Bøvik Larsen, for the proposal of the thesis in first place, for the support with needed articles and books, and for the encouragement with useful hints and tips throughout the thesis work.

A special thank goes also to my family, that gave me the possibility to carry out my studies through all these years and gave me the idea to make the experience of studying abroad.

A note of mention also to:

- Casa Gio, an Italian restaurant in Stavanger where I worked as a part-time during the studies, giving me the chance to self-finance my stay in Norway
- ISU Stavanger, huge help in the integration with the other fellow students
- Poviglio Baseball team, the baseball team where I have played for 12 years in Italy

Matteo Busi 15 June 2016

Short Summary

Variation of the absorption properties as a function of energy across, or near, an absorption edge is known as EXAFS (Extended X-ray Absorption Fine Structure). This technique implies scanning over an absorption-edge and simultaneously record the (fluorescent in this case) signal by a suitable detector. This signal contains, among other things, information of the local chemical coordination (interatomic distances etc.) of the compound observed. It is a well-known and much used technique. However, one issue which has not been considered well enough, is the question of influence by the sample geometry. As a first approximation one always assumes a sample of "infinite size", or only one finite thickness parameter. The department's research group, has been working with improving this, by taking into consideration the sample geometry in terms of a cylinder or a sphere. The theory dealing with these geometries has been established. There was also collected absorption coefficient's data sets for this, using copper sulphate as the reference sample. The purpose of the work is to analyze the data sets and perform the developed self absorption corrections and evaluate whether it is possible to establish a new correction tool. The data processing and the execution of the correction models confirm the dependency of the self-absorption effect on parameters such as concentration and thickness (by inner radius) of the sample, and a good agreement between the first order approximation and complete numerically evaluated corrections for both spherical and cylindrical cases.

Contents

1

Introduction

1.1 Background

The use of Synchrotron Radiation as a powerful research tool in science has grown rapidly in the past few years. Vacuum and X-ray photons emerging from storage rings are today among the most frequently used probes for the investigation of the electronic and geometric structure of matter. Synchrotron Radiation by its nature has stimulated interdisciplinary efforts with its applications ranging wide through many fields. Several experimental techniques and methods were developed taking advantage of this technology as:

- XPS (X-Ray photo-emission spectroscopy): used to probe the surfaces of materials. Some recent application of this can be found in the references [47, 48]
- XRD (X-Ray diffraction) based experiments such as XRT (X-ray topography) and innovative ones such as µXRD (Micro X-Ray diffraction). A few examples of these are found in [42, 46]
- Soft X-ray optics and microscopy: to overcome the impossibility of fabricating X-ray lenses. A good review is found in a recent study [49]
- XRL (X-Ray Lithography): used for example to create Computer's chipsets. An interest work demonstrating its potential as next generation lithography can be found in [45]
- EXAFS and XANES, which are going to be discussed deeply in the following chapters

The rise of these useful methods helped researchers of many fields, ranging from chemistry, to medicine and astrophysics [34] and more, to carry out their studies. In the work which is going to be presented the focus will be on the EXAFS method, to provide a general introduction to its basics, and to improve the solution to a frequent problem experienced in the measurement: the self-Absorption effect. This is a phenomenon that happens during the measurements and dampens the intensity of the signal. In the past many attempts were done to overcome this problem, and most of them are based upon the "thin sample" limit,

that will be discussed later. In 2013 an article providing the theoretical models to develop a method to correct the geometry of the sample was published [43]. This is an aspect that had never been considered before, but in fact it was theoretically proven that the shape of the sample has a contribution to the self-absorption effect.

1.2 Objectives

In the previous section it was introduced the problem of the geometry of the sample to be examined, and its theoretical correction method. After the theoretical models had been published, experimental tests were carried out in Grenoble (France), using the accessibility to a Synchrotron Radiation. The sample to be observed was a liquid solution of copper sulphate pentahydrate ($CuSO_4 \cdot 5\,(H_2O)$) contained in a cylindrical capillary and a solid state sphere of the same compound. There were also two parameters for the sample to be studied: the concentration (measured as Molarity), and the width of the sample (measured as the radius of the cylinder and the sphere). EXAFS data were then collected with the fluorescence technique. In this thesis work, this will be starting point, with the following objectives:

- Getting familiar with a software dealing with absorption data to calculate and visualize the EXAFS spectra in the proper spaces.
- Make comparisons with the different samples measured.
- Perform the developed correction regarding the geometry sample and to find out whether it is possible to fully correct it.
- Discuss the results and their consequences to enhance future measurements.

1.3 Outline of the report

This report is so structured:

There will be a brief summary of the background theory describing the experiment and the measured quantities involved in chapter 2. It will follow a deep description of EXAFS and the self-absorption problem in chapter 3 including an overview of the corrections model. In chapter 4 is then pictured the experimental setup continued by the processing and analysis of the provided raw data and its linked execution of the correction routines in chapter 5. In chapter 6 the result obtained are discussed and conclusions are drawn.

2

X-Ray Absorption

This chapter will highlight the necessary theory background to describe the experiment and the EXAFS technique. The content, including figures and equations, is highly inspired by the books [50, 51] and the review of XAFS of Matthew Neville [52].

2.1 Photoelectric Absorption

The use of the X-Ray absorption has nowadays taken part of the daily life. It can almost safely be said that everybody in their life has benefited at least once of it. One of the most common way is for example the X-Ray cross section of the bones to check whether a fracture is present. This application relies on the transmission property of the X-Ray beams to be highly dependent on the atomic number Z (approximately to the fourth power), this in fact implies a neat contrast between materials of different densities, in this case bones and tissue. Moreover, the penetrating power of the beam varies with its energy, ε, roughly as $\frac{1}{\varepsilon^3}$ giving the possibility to adjust to the suitable penetration depth. Consider now a sample of thickness r in a transmission experiment where the intensities are measured with (I_0) and without (I) the sample. It is called the transmission T:

$$T = \frac{I}{I_0} = e^{-\mu r} \tag{2.1}$$

where it's introduced the absorption coefficient μ :

$$\mu = (\frac{\rho_m N_A}{A})\sigma_a$$

What is called σ_a is defined as absorption cross-section per atom, and is related with the absorption coefficient by Avogadro's number, mass density and molar mass; respectively N_A, ρ_m and M.

While figure 2.1 shows the dependency of the absorption cross-section on Z and ε for different elements, it is also useful to introduce the concept of absorption edges, which is crucial in this work later on. These are

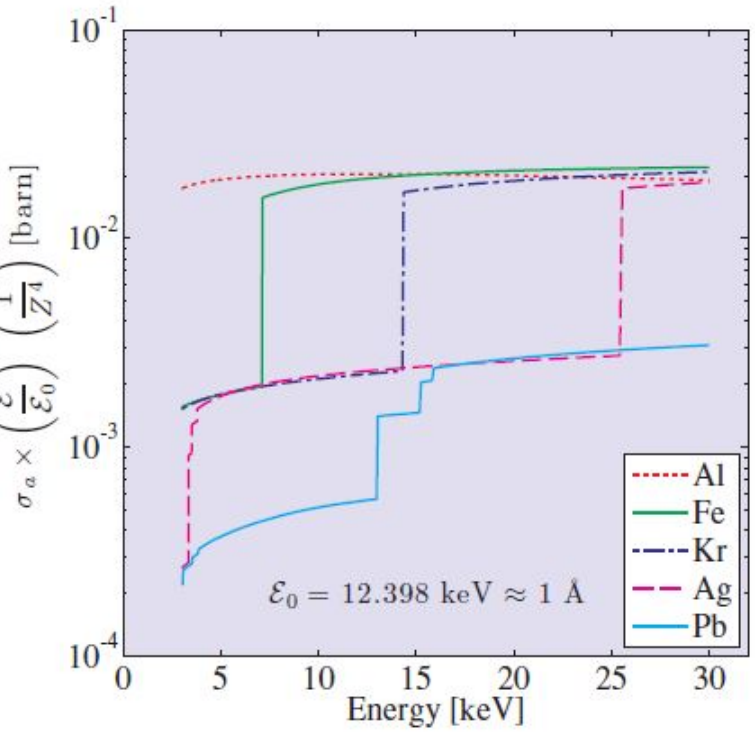

Figure 2.1: A plot of the absorption cross-section for various elements. It is multiplied by the reciprocal of the atomic number at the fourth power and the ratio between the energy of the beam and ε_0 taken as 1 Å. Figure adapted from [51].

represented by the discontinuous jumps at element specific energies in the absorption cross-section. Electrons are bound to atoms with discrete energies ε_b, when the energy of the photon ε_p becomes greater ($\varepsilon_p > \varepsilon_b$), the photon can interact with the atom removing one of the shell atoms in the process, with the photon being annihilated. This is the so called phenomena of the Photoelectric Absorption. When the energy of the photon is instead less ($\varepsilon_p < \varepsilon_b$) this is not possible, one of the photoelectric channels closes and the absorption cross-section falls by a certain amount.

It will now follow a subsection describing the quantum mechanical treatment to find an expression for the absorption cross-section.

2.1.1 Quantum mechanical treatment

The scattering event in quantum qechanics is defined by the time-dependent perturbation theory. The interaction between the incoming beam and the sample is then defined by the Hamiltonian of interaction, $\mathcal{H}_I$, as transition from an initial ($|i\rangle$) to a final state ($|f\rangle$). It is also given in first-order perturbation theory by Fermi's Golden Rule, the number of transitions per second W :

$$W = \frac{2\pi}{\hbar}|M_{if}|^2\rho(\varepsilon_f)$$

with the matrix element $M_{if} = \langle f|\mathcal{H}_I|i\rangle$ and $\rho(\varepsilon_f)$ being the density of the states.

The absorption process is not elastic, meaning the incident photon expels an electron from an atom with binding energy ε_b. $\varepsilon_{pe} = \frac{\hbar^2 q^2}{2m}$ is instead the kinetic energy of the photo-electron and is equivalent to the difference between ε and ε_b with ε the incident photon. In this case there are no restrictions over the direction of the wave vector of the photo-electron, $\vec{q}$, and thus is enough to perform the integration over the entire solid angle of $\Delta\Omega = 4\pi$.

$$W_{4\pi} = \int \frac{2\pi}{\hbar} |M_{if}|^2 \rho(\varepsilon_{pe}) \delta(\varepsilon_{pe} - (\varepsilon - \varepsilon_b))\, \mathrm{d}\varepsilon_{pe}.$$

The density of states for the photo-electron is evaluated in the same way as for scattering events, using the so called box normalization [51].

$$\rho(\varepsilon_{pe}) = 2\left(\frac{V}{8\pi^3}\right)\left(\frac{\mathrm{d}\mathbf{q}}{\mathrm{d}\varepsilon_{pe}}\right)$$

Here the factor 2 allows for the two possible spin states of the electron, while the volume element $\mathrm{d}\mathbf{q}$ is replaced by $q^2 \sin(\theta)\mathrm{d}q\mathrm{d}\theta\mathrm{d}\phi$. It is now possible to define the absorption cross-section as:

$$\sigma_a = \frac{W_{4\pi}}{\Phi_0} = \frac{2\pi}{\hbar c}\frac{V^2}{4\pi^3}\int |M_{if}|^2 \delta(\varepsilon_{pe} - (\varepsilon - \varepsilon_b))\, q^2 \sin(\theta)\mathrm{d}q\mathrm{d}\theta\mathrm{d}\phi. \tag{2.2}$$

with $\Phi_0 = c/V$ the incident flux. It is also now defined the factor M_{if} (calculation details can be retrieved in book [51]) as:

$$M_{if} = \langle f|\frac{e}{m}\mathbf{p}\cdot\mathbf{A}|i\rangle$$

Here are introduced the terms $\mathbf{p}$ and $\mathbf{A}$, the momentum operator and vector potential, coming from the interaction Hamiltonian $\mathcal{H}_I$. The expression is then obtained by neglecting the coulomb interaction between the photo-electron on the positively charged ion left behind (i.e. free electron approximation).

2.2 Free-electron approximation

It is now briefly reported the derivation of the free-electron approximation for the calculation of the absorption cross-section (full treatment can be read in [51]). The initial state $|i\rangle$ is defined as one photon described by the couple $(\mathbf{k}, \hat{\boldsymbol{\varepsilon}})$ being respectively its wave-vector and its polarization, and one K electron: $|i\rangle = |1\rangle_x|0\rangle_e$. The final state $|f\rangle$ is represented instead by the annihilated photon and the photo-electron expelled by the absorption process: $|f\rangle = |0\rangle_x|1\rangle_e$. It is then found the state for which the electron is free as eigenfunction of $\mathbf{p}$ with eigenvalue $\hbar\mathbf{q}$:

$$M_{if} = \frac{e\hbar}{m}\sqrt{\frac{\hbar}{2\epsilon_0 V\omega}}(\mathbf{q}\cdot\hat{\boldsymbol{\varepsilon}})\int \Psi^*_{e,f} e^{i\mathbf{k}\cdot\mathbf{r}}\Psi_{e,i}\,\mathrm{d}\mathbf{r}$$

where $\mathbf{r}$ is the position vector of the photo-electron and Ψ its wave-function. The square root term is the normalization factor A_0, that turns out from the quantization of the vector potential $\boldsymbol{A}$. It is now considered for the approximation that the initial wave-function of the electron is taken to be that of the 1s bound state,

while the final wave-function is of a free electron. These conditions are written respectively as:

$$\psi_{e,i} = \psi_{1s}(\mathbf{r})$$

and

$$\psi_{e,f} = \frac{1}{\sqrt{V}} e^{i\mathbf{q}\cdot\mathbf{r}}$$

It is also defined the wave-vector transfer by $\boldsymbol{Q} = \boldsymbol{k} - \boldsymbol{q}$, and its integral as $\phi(\boldsymbol{Q})$, the Fourier transform of the wave-function of the electron in its initial state. This makes possible to evaluate the squared matrix element,

$$|M_{if}|^2 = \left(\frac{e\hbar}{m}\right)^2 \frac{\hbar}{2\epsilon_0 V^2 \omega} (q^2 \sin\theta^2 \cos\phi^2) \Phi^2(\boldsymbol{Q})$$

and thus the absorption cross-section per K by a substitution of the matrix element in the equation:

$$\sigma_a = \left(\frac{e\hbar}{m}\right)^2 \frac{1}{4\pi^2 \epsilon_0 c\omega} I_3$$

where I_3 is a three-dimensional integral, about which definition and evaluation is skipped for convenience (however it can be found in the literature [51]), however it is found to be reduced to the quantity $(\frac{4}{3})[\frac{\omega_A^2}{\omega\omega_c}]^{5/2}$.

Now the following quantities are defined as:

- $\hbar\omega_K$: The energy of the absorption edge, proportional to Z^2 for a simple model
- $\hbar\omega_A$: The energy related to κ, the inverse length scale of the wave-function ψ_{1s}, proportional to Z
- $\hbar\omega_c$: The highest characteristic energy, defined as: $\hbar\omega_c = 2mc^2$

and show the final result for the atomic absorption cross-section per atom:

$$\sigma_a = 32\lambda r_0 \left(\frac{4}{3}\right) \left[\frac{\omega_A^2}{\omega\omega_c}\right]^{5/2} \quad \text{for } \hbar\omega_K << \hbar\omega << \hbar\omega_c$$

This makes apparent that the absorption cross-section varies as Z^5 via ω_A, and as $\omega^{-7/2}$ via the factor of $\lambda = 2\pi c/\omega$. This result is slightly different from the experimental findings, summarized in Fig. 2.1. The reason for this difference is caused by the approximation made for the free-electron, implying the Coulomb interaction between the photo-electron and the positively charged ion to be neglected. However in this way, it was available to obtain an analytical approximate expression for σ_a.

2.2.1 Beyond the free-electron approximation

In this chapter it will be shown a further step in the calculation of the absorption cross-section. By the purpose of this report the result from Stobbe in the 1930 [10] will be stated without proof. He introduced

the dimensionless photon energy variable:

$$\xi = \sqrt{\frac{\omega_k}{\omega - \omega_k}}$$

and it is conveniently possible to write his result as a correction factor $f(\xi)$ for the absorption cross-section per K electron:

$$\sigma_a = 32\lambda r_0 \left(\frac{4}{3}\right) \left[\frac{\omega_A^2}{\omega\omega_c}\right]^{5/2} f(\xi)$$

This correction factor is dependent on both Z and $\hbar\omega$, and its explicit form can be written as:

$$f(\xi) = 2\pi\sqrt{\frac{\omega_k}{\omega}} \left(\frac{e^{-4\xi \operatorname{arccot} \xi}}{1 - e^{-2\pi\xi}}\right)$$

It is useful at this point to consider two interesting limits:

1. When the photon energy is greater than the binding energy: $\hbar\omega \gg \hbar\omega_k$ or $\xi \to 0$, it follows that $f(\xi) \to 1$.

   This returns the same result for the free-electron approximation: if the photon energy is high, so is the energy of the photo-electron and it makes a little difference if it is free to move, or it is in a weak attractive field produced by the positive ion.

2. When the photon energy is approaching a threshold energy: $\hbar\omega \to \hbar\omega_k^+$ or $\xi \to \infty$, if follows that $f(\xi) \to \frac{2\pi}{e^4}$

   At the threshold energy there is thus a discontinuous jump of:

$$\sigma_a = 32\lambda r_0 \left(\frac{4}{3}\right) \left[\frac{\omega_A^2}{\omega\omega_c}\right]^{5/2} \left(\frac{2\pi}{e^4}\right)$$

To calculate the values for ω_A and ω_K, needed for the evaluation of the energy dependence and the step height in σ_a at the K edge, it is used the approach of hydrogen atom. In this way the K shell ionization of an atom with Z electrons is approximately the binding energy of the hydrogen atom times Z^2: $\hbar\omega_K = Z^2e^2/\pi\epsilon_0 2a_0$, while $\hbar\omega_A = Z\hbar c/a_0$.

It is therefore possible to write the edge jump per K electron as:

$$\sigma_a(\lambda_K) \simeq \left(\frac{256\pi}{3e^4}\right) \lambda_K r_0 \tag{2.3}$$

and the energy dependence as:

$$\sigma_a \simeq 32\lambda r_0 \left(\frac{4}{3}\right) \left[\frac{\omega_K}{\omega}\right]^{5/2} \left(\frac{2\pi}{e^4}\right) \tag{2.4}$$

The results shown in Eqs.(2.3) and (2.4) are proven to be reliable, as compared to recent experiments and more detailed and refined frameworks, for example within the self-consistent field Dirac-Hartree-Fock [30].

2.3 X-Ray Fluorescence

It is also useful to introduce the concept of X-Ray fluorescence. It is explained recalling now the photoelectric absorption introduced earlier. In this process, an X-ray photon is absorbed and an electron ejected from the atom creating a hole in the inner shell. Therefore the absorbing atom is said to be in an excited state, consisted by a core-hole and a photo-electron. This state subsequently decays within a lapse of few femtoseconds. However there are two ways schematized in Figure 2.2 that this can happen:

1. Auger Effect: An electron with higher energy fills the lower energy hole created, with a subsequent release of another electron, called Auger Electron, from the same atom. The Auger emission was first observed and published in 1922 by Lise Meitner[5]. It is the basis of the Auger Electron Spectroscopy (AES), a surface analysis technique.

2. X-Ray Fluorescence: One of the electrons in an outer shell fills the hole, with emission of an electromagnetic wave. This is an X-ray emission as the photon is in that energy range. Depending on the shell of the electron the fluorescent radiation are referred as lines. This process is the basis of the X-Ray Absorption Spectroscopy (XAS) in the fluorescent regime.

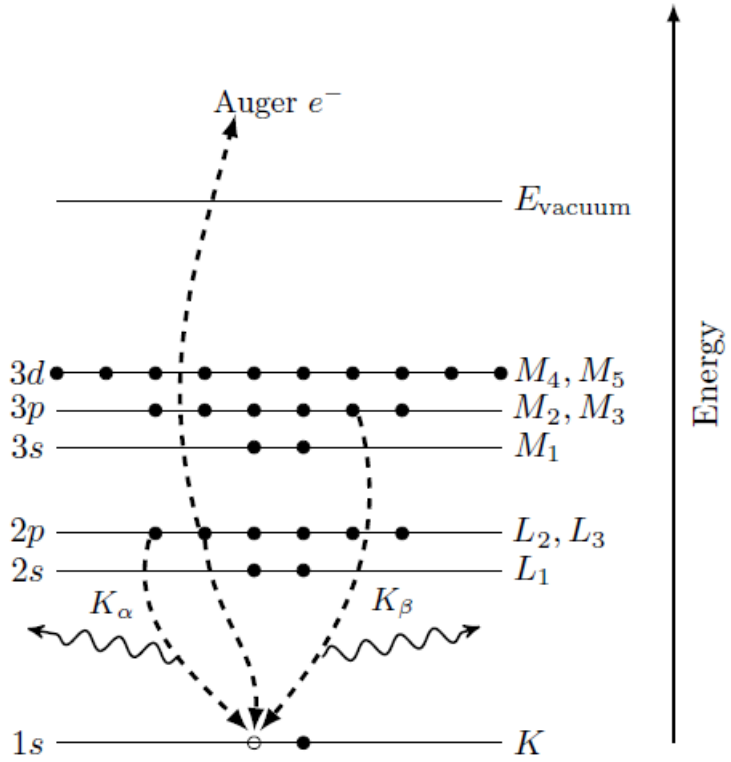

Figure 2.2: The excited state can decay by either X-Ray fluorescence or the Auger effect. In both cases an electron drops first from a higher level to fill the hole provoked by X-Ray incidence. The energy difference between the two levels is then transmitted to the emitted particle, that can be an electron for Auger effect, or an X-Ray emission for the fluorescence (K_α and K_β lines). Figure taken from [52].

3

XAFS (X-Ray Absorption Fine Structure)

In X-Ray Absorption Spectroscopy, the absorption coefficient μ is measured by variating the energy of the incident X-Ray beam giving rise to the absorption spectra. A typical XAFS spectra is shown in Fig. 3.1 and depending on the chemical properties subject of the study, two different regimes are distinguished:

1. XANES (X-Ray Absorption Near Edge Spectroscopy): includes the absorption edge and a few eV-s in its proximity. It describes the oxidation state and the coordination chemistry of the sample. Some notable works revolving around this technique can be found in literature [21, 33].

2. EXAFS (Extended X-Ray Absorption Fine Structure): includes a greater range of eV-s above the absorption edge. It describes information as the atomic distances, coordination number and species of atoms neighboring the absorber.

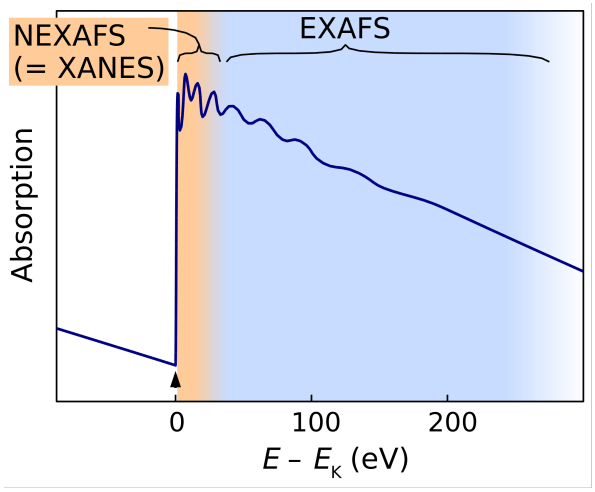

Figure 3.1: A typical XAFS absorption spectra. It is also shown the localization of XANES and XAFS regimes.

For the purpose of this work, the focus will remain on the EXAFS regime, examining its limits and defects, and a way to solve or minimize them.

3.1 EXAFS

3.1.1 Historical Development

A detailed overlook on the development of the EXAFS technique is accurately found in the work by Stern [20]. Here some of the major steps that brought it to how we know it today are reported.

The first experimental detection of fine structure far above the absorption edges were by Fricke and Hertz in 1920 [1, 2]. The first structure detected was the near edge structure (Coster 1924 [6], Lindh 1921[4], 1925 [7]) which could be explained by the theory of Kossel (1920) [3]. However, evidences of oscillations in the extended range of a few eV-s above the absorption edge as in the experiment of Ray in 1929 [8], Kievet and Lindsay in 1930 [9], brought the need of an explanation of this extended fine structure. The temperature dependence in EXAFS was first noted experimentally by Hanawalt in 1931 [11]. With the new theoretical background brought by quantum mechanics Kronig attempted to explain the EXAFS in condensed matter in his work in 1931 [12]. His theory relied on the concept of the energy gaps at the Brillouin zone boundaries and thus depended explicitly on the long range order in the solid. Following the publication of Azaroff in 1963 [14], this theory was called a Long Range Order (LRO) theory, and the other class of theories Short Range Order (SRO). Even though LRO theory was in error it took many years before its deduction by Stern, in 1974 [15]. This was done by introducing the mathematical tool of the Fourier transform to give an interpretation of the EXAFS function χ, defined later in eq. (3.1) by means of distance corresponding to the path from the absorber to the nearest neighbor coordination shells of atoms.

3.1.2 Theoretical Description

Is has been shown in the previous chapter how the absorption of X-Rays can be a powerful tool for the determination of the arrangements of atoms. However by the studies through samples in different situations it became clear that the absorption has a remarkable dependence on the environment of the absorbing atom. For example as it is shown in Fig. 3.2 , the 2D crystalline Krypton sample, displays oscillations in its absorption spectra that cannot be seen in its gaseous phase.

This discrepancy can be physically explained by considering again the photo-electron liberated in the absorption as an outgoing spherical wave, the presence of neighboring atoms cause this wave to be scattered back. The interference between the outgoing and the back-scattered wave give rise to the oscillations that are referred as the Extended X-Ray Absorption Fine-Structure (EXAFS) effect. By its definition, EXAFS's purpose to describe the fine structure of the sample studied by obtaining the location of the first few nearest

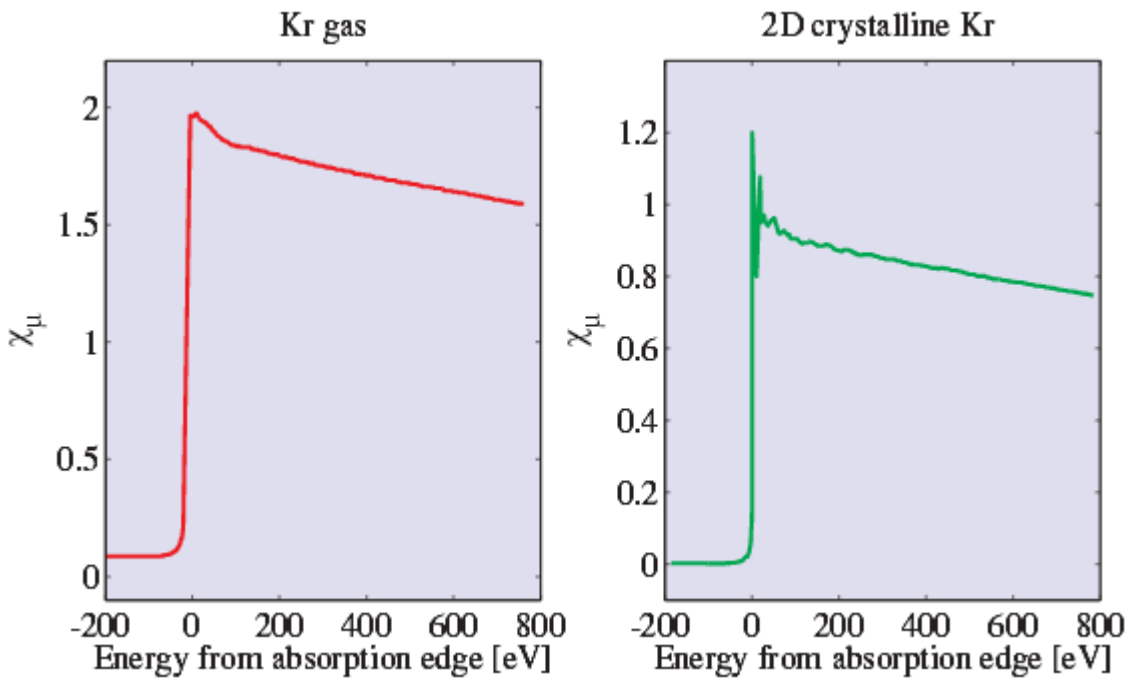

Figure 3.2: A comparison of the Krypton absorption spectra in its gaseous form and a crystalline sample. EXAFS oscillations are detected in the 2D crystalline Kr. Figure adapted from [51].

neighbor atoms surrounding the absorbing one. It is mathematically introduced as:

$$\chi(E) = \frac{\mu_t(E) - \mu_X(E)}{\Delta\mu_X(E)} \tag{3.1}$$

with $\mu_t(E)$ being the measured total absorption coefficient, $\mu_X(E)$ the absorption coefficient the isolated absorbing atom and the $\Delta\mu_X(E)$ in the denominator is the absorption jump in order to have the EXAFS function normalized. Figure 3.3 displays how the EXAFS is calculated in Eq.(3.1).

3.1.3 Quantum Mechanical treatment

In the previous chapter it has been built a relatively simple model of the photo-electron process, capable of accounting for the main features of the absorption cross-section of an isolated atom. To describe the EXAFS effect we start from what it was achieved in Chapter 2, where it was shown in Eq.(2.2) the absorption coefficient dependence from the interaction term:

$$\mu(E) \propto |\langle i|H|f\rangle|^2$$

The initial state $|i\rangle$ describes the very inner electrons in absorbing atoms, and thus are not modified when considering EXAFS oscillations. They must then arise from the final state, so that $|f\rangle \rightarrow |f_0 + \Delta f\rangle$, with $|f_0\rangle$

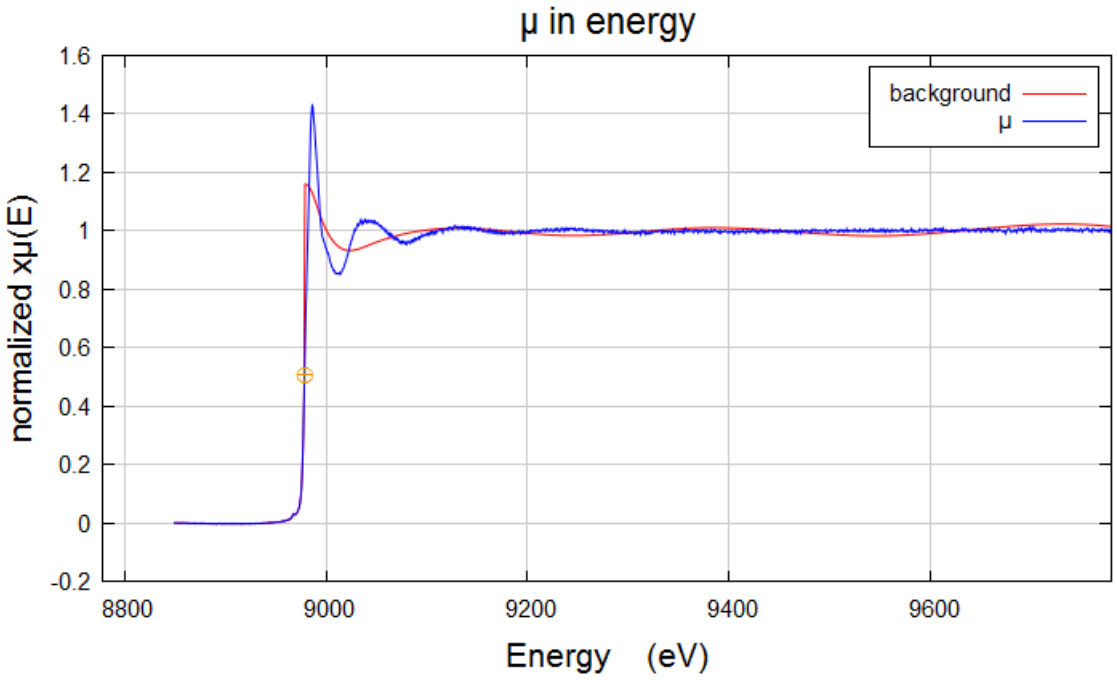

Figure 3.3: Obtained spectra of the normalized absorption coefficient of a $CuSO_4$ penta-hydrate solution in cylinder capillary. The blue line represent the measured absorption coefficient $\mu(E)$ while the red line is a smoothed background function interpreted as $\mu_0(E)$. The yellow crossed circle is represent the absorption edge location.

the final state of the free atom and $|\Delta f\rangle$ a small modification representing the EXAFS. So that μ becomes:

$$\mu(E) = \mu_0(E)\,[1 + \chi(E)]$$

with $\mu_0 = |\,\langle i|H|f_0\rangle\,|^2$ representing the bare atom, and $\chi(E) \propto \langle i|H|\Delta f\rangle$ representing the fine structure. Starting from this point it can be found an initial simple expression for the EXAFS, the initial state $|i\rangle$ is approximated by delta function $\delta(r)$, the interaction term H is reduced by a term proportional to e^{ikr}, while the change in the final state is the wave-function of the scattered photo-electron, $\psi_{scatt}(r)$:

$$\chi(E) \propto \int \delta(r) e^{ikr} \psi_{scatt}(r)\,\mathrm{d}r$$

This states that the EXAFS is proportional to the amplitude of the scattered photo-electron at the absorbing atom, $\psi_{scatt}(0)$. For the extrapolation of the chemical properties is then useful to space shift $E \to k$ by $k = \sqrt{\frac{2m}{\hbar^2}(E - E_0)}$ [1] with E_0 the absorption edge energy, the outgoing photo-electron wave function is now described as

$$\psi(k, r) = \frac{e^{ikr}}{kr} \tag{3.2}$$

[1] This step makes crucial the accuracy in the choice of the absorption edge of the absorber E_0. $\chi(k)$ is also usually k-weighted to minimize the systematic error and to better display the oscillations in the extended range. Weights used range from 1 to 3 ($k\chi(k)$,$k^2\chi(k)$,$k^3\chi(k)$) and 2 is usually preferred.

it travels a distance R_j to the neighboring j-atom, then it scatters back to the absorbing atom, still as a spherical wave. By putting all these factors together, the EXAFS equation is obtained as it reads:

$$\chi(k) = \sum_j \frac{N_j e^{-2k^2\sigma_j^2} f_j(k)}{kR_j^2} \sin\left[2kR_j + \delta_j(k)\right] \tag{3.3}$$

where it have been introduced $f(k)$ and $\delta(k)$ as scattering properties of the neighboring atom depending on Z; N as the coordination number; σ^2 as the mean-square-displacement in the bond distance R. It is important to be noted that all the j neighboring atoms are considered as identical and equidistant R_j from the absorber. Details of these terms are described in Appendix A.

3.1.4 Refining the model

In order to get a more refined equations for the EXAFS, some aspects that were previously neglected have to be considered.

Inelastic mean free path

In order to participate in the XAFS, the photo-electron has to scatter from the neighboring atom and return to the absorber elastically as the outgoing photo-electron. However, in Eq.(3.2) it was neglected that the photo-electron can also scatter inelastically from other sources (like conduction electrons, phonons...). Moreover the photo-electron has to return to the absorber before the excited state decay (this lapse of time is called core-hole lifetime). To account for this Eq.(3.2) is modified to:

$$\psi(k,r) = \frac{e^{ikr} e^{-2r/\ell(k)}}{kr}$$

with ℓ being the mean-free-path of the photo-electron. In this way the EXAFS Eq. (3.3) becomes:

$$\chi(k) = \sum_j \frac{N_j e^{-2k^2\sigma_j^2} \; e^{-2R_j/\ell(k)} \; f_j(k)}{kR_j^2} \sin\left[2kR_j + \delta_j(k)\right] \tag{3.4}$$

three important consequences emerge from this equation. First of all by the $\ell(k)$ and R^{-2} terms, it follows that XAFS is a local probe, not seeing further than approximately a distance of 5 Å
from the absorbing atom. Secondarily, the XAFS oscillations will consist of different frequencies, corresponding to a distinguished distance for each coordination shell, leading to the need of Fourier transforms. Finally, accurate values for the scattering amplitude and phase-shifts $f(k)$ and $\delta(k)$ are needed in order to extracts the relevant properties of the sample.

Intrinsic losses

This involves another approximation made in description above, which was ignoring the relaxation due to the other electrons in the excited atom. This can be solved by introducing a new factor:

$$S_0^2 = |\langle \Phi_f^{Z-1} | \Phi_0^{Z-1} \rangle|^2$$

accounting for the remaining $Z-1$ electrons in the initial and final state. This term, although it may have some k-dependence, is considered to be a constant term, therefore it can be added to Eq. (3.4) to obtain:

$$\chi(k) = \sum_j \frac{S_0^2 N_j e^{-2k^2\sigma_j^2} e^{-2R_j/\ell(k)} f_j(k)}{kR_j^2} \sin\left[2kR_j + \delta_j(k)\right] \tag{3.5}$$

A consequence of this factor is to be completely correlated with the coordination number N, making its extrapolation hard to be determined with high accuracy.

Multiple scattering

Another simplification assumed so far, was that the photo-electron scattering from the neighboring atom always returns back to the absorbing atom. However in a more realistic scenario the photo-electron can actually scatter from multiple neighboring atoms, giving rise to more complex scattering patterns.

This aspect has consequences that are more important in XANES, but can be present in EXAFS as well, especially beyond the first coordination shell. Anyways since most of EXAFS studies are restrained to the first coordination shell, more details on this are left to further readings [35].

Disorder terms

In Eq. (3.3) the disorder was described using the term $Ne^{-2k^2\sigma^2}$, however the core-hole life time is in the femto-second range, much smaller than the thermal vibrations which are in turn in the pico-second range. This means that each X-Ray absorbed in an EXAFS measurement gives a "snapshot" of the structure around a randomly selected absorbing atom in the sample, with the neighboring atoms in a frozen configuration. Therefore when the spectrum is built, the result will be a "blurred picture" composed by many of these snapshots. Then by consequence a single EXAFS measurement cannot distinguish thermal disorder due to atomic vibrations from static disorder.

An EXAFS measurement is then a sampling of the configuration of atoms around the average absorbing atom, that is usually given by the Partial Pair Distribution function, $g(R)$, which gives the probability that an atom is found a distance R away from an atom of the selected type. Pair distribution functions are found from many structural probes (notably scattering techniques), but the Partial aspect is unique to EXAFS since as discussed above it is a local probe, sensitive to only the atom pairs which includes the absorbing one.

A good example of modeling the complex disorder by a parametrization of $g(R)$ can be found in the work of Filipponi et al. [31].

In the present work it will be continued to use N and σ^2, however it has been shown that more complex descriptions of the distribution of atoms can be used.

3.2 XAFS Measurements

Throughout the research progress in the XAFS measurements, two main techniques were established and developed, depending on the nature of the sample subject of studies: transmission and fluorescence. In both cases the X-Ray source is a synchrotron, as it provides a full range of X-Ray wavelengths and a monochromator that, using Bragg diffraction, is able to select a particular energy with sufficient accuracy.

Transmission

In the transmission technique the absorption coefficient introduce in Eq.(2.1) is measured for the sample as:

$$\mu(E) = \log \frac{I_0}{I}$$

It is usually preferred when dealing with highly concentrated samples. In order to get enough transmission to pass through the sample, the thickness ($t = \log[I/I_0]$) is adjusted to be so that $\mu t \approx 2.5$ above the absorption edge. Another requirement for a accurate measurement is having an uniform sample, free of pinholes; for a powder, the grain size must be smaller than the absorption length.

3.2.1 Fluorescence

For measurements made in fluorescence regime, the absorption coefficient defined in Eq.(2.1) is instead found as:

$$\mu(E) \propto \frac{I_f}{I_0} \tag{3.6}$$

with I_f the intensity of the fluorescent line provoking the X-Ray emission. It is a technique preferred in case of thick and diluted samples as it gives more accurate measurements.

During fluorescence XAFS measurements, the X-Ray emitted includes the fluorescent line of elements of interest, but of other elements present in the sample, and both elastically and inelastically scattered X-Rays (Compton). This has the consequence of requiring two main aspects to be considered. First of all the need of the solid angle, as the fluorescence is emitted isotropically, and it's preferred to maximize the signal detected. The scatter instead, is not emitted isotropically but is polarized in the plane of synchrotron. Therefore by placing the detector normal to the incident beam, most of the elastic scatter is suppressed, and this is the position preferred for the detectors.

Secondarily the energy discrimination also plays an important role as it can allow to completely suppress fluorescent lines from elements not of interest. This aspect is principally solved by use of manufactured filters or innovative solid-state detectors [19, 25].

3.3 Self-Absorption Effect

What is left to analyze before focusing on the experiment is to consider one of the most important effect influencing measurements performed with Fluorescent X-Ray Absorption Spectroscopy (FlXAS), the so called 'self-absorption' effect. The name it has been given is quite tricky because it doesn't refer to the fact that the emitted fluorescent X-Rays are absorbed by the sample itself, that is an important factor to be considered in cases where a diluted element is placed in a dense matrix. In the context of this work and the majority of the X-Ray spectroscopy field it instead refers to changes in the mean absorption depth with the energy of the incident photon (ε), which changes the probability of the fluorescence photon to be reabsorbed by the sample being scanned. The resulting effect is an attenuation the absorption spectra as it can be observed in Figure 3.4, that affect all kind of samples and it is thus more interesting to study.

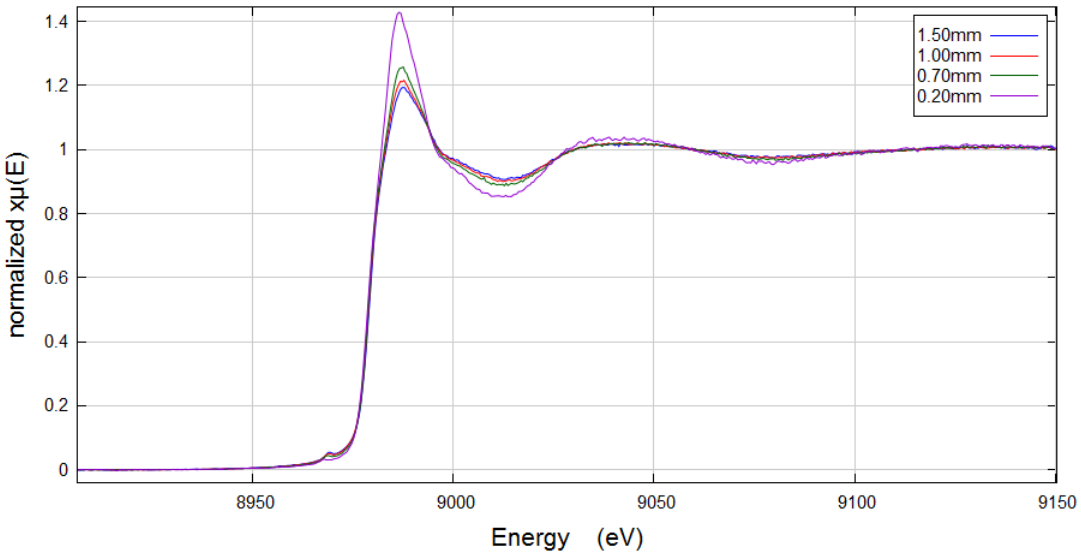

Figure 3.4: A plot of the normalized absorption coefficient $\mu(E)$. The sample is a liquid copper sulphate $CuSO_4$ pentahydrate of concentration 1M, placed in a cylindrical capillary of different inner radius. As the sample gets thicker the amplitude of the oscillations is more attenuated. More details about this are described in chapters 4 and 5.

The starting point for a mathematical definition of the Self-Absorption effect is (3.6). That was actually an oversimplification. Since all matter attenuates X-Rays, I_f and $\chi(E)$ can be damped. The measured I_f is

then written as:

$$I_f = I_0 \frac{\epsilon \Delta\Omega}{4\pi} \left[\frac{\mu_X(E) \left(1 - e^{-\left[\frac{\mu_t(E)}{\sin\theta} + \frac{\mu_t(E_f)}{\sin\phi} \right] r} \right)}{\frac{\mu_t(E)}{\sin\theta} + \frac{\mu_t(E_f)}{\sin\phi}} \right] \tag{3.7}$$

with ϵ the fluorescence efficiency, $\Delta\Omega$ the solid angle of the detector, θ and ϕ the incident and exit angle respectively (Fig. 3.5). It is also useful to remind that μ_t has contribution to both the absorption of the element of interest μ_X, and all the rest μ_b; $\mu_t = \mu_X + \mu_b$.

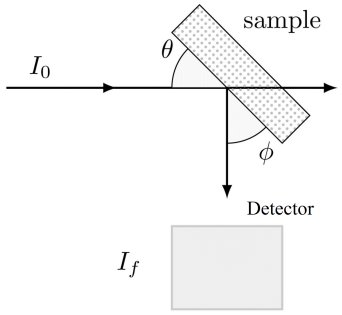

Figure 3.5: The geometrical model used to obtain Eq. (3.7).

It will now be examined some limits that represent the ideal measurement conditions.

Thin sample limit

A first limit to examine of Eq. (3.7) is the case of the thin samples (i.e. $\mu r << 1$).

A Taylor expansion of the exponential term cancels the denominator so that:

$$I_f \approx I_0 \frac{\epsilon \Delta\Omega}{4\pi} r \mu_X(E) \tag{3.8}$$

Thick and dilute sample

In the case of thick ($\mu r >> 1$) and dilute ($\mu_X << \mu_b$) samples, the exponential term goes to 0, and the energy dependence of μ_t can be ignored so that:

$$I_f = I_0 \frac{\epsilon \Delta\Omega}{4\pi} \frac{\mu_X(E)}{\frac{\mu_t(E)}{\sin\theta} + \frac{\mu_t(E_f)}{\sin\phi}} \approx I_0 \mu_X(E) \tag{3.9}$$

Grazing exit limit

Another way to reduce the self absorption effects for thick and concentrated samples is, by looking at Eq. (3.7), is to play with the exit angle. If it is possible to rotate the sample such that it is nearly normal to the

incidence angle, then $\phi \to 0$ and thus $\frac{\mu_t(E_f)}{\sin\phi} >> \frac{\mu_t(E)}{\sin\theta}$. Therefore it's obtained:

$$I_f \approx I_0 \frac{\epsilon\Delta\Omega}{4\pi} \frac{\mu_X(E)}{\frac{\mu_t(E_f)}{\sin\phi}} \tag{3.10}$$

However, in the majority of situations these requirements cannot be satisfied, leading to a interest in the development of enhanced self-absorption corrections.

3.3.1 Self-absorption corrections

The first signs and studies about this dates back to the period of the 80's with the publication of J.Goulon [22] which was interested in the details caused by the complexity of an accurate extrapolation of the coordination number and Debye-Waller factor of the absorber neighbors. Later studies in the 90's [27, 29, 36] provided sensible results for the corrections of this factor, making use of two important assumptions. The first one is actually needed in order to make the correction factor analytical, that consist in a replacement of the true absorption coefficients with their average values. This means that the modulating effect of χ on the correction factor is expected as very small. A second assumption is the so called 'thick limit', that eliminates the dependence on the sample thickness with downsides being limited to thick and concentrated samples, like single crystals. The work of Tan, Budnick and Heald [27] is an exception that rather than correcting the data uses other assumptions to directly estimate the attenuation factors to the amplitude reduction factor, S_0^2, and to the Debye-Waller factors, σ^2. A successful attempt to go beyond the thick-limit is published in 2005 by Booth and Bridges [38] and with only one assumption proved to be nearly exact in most of measurement cases, corrects fluorescence EXAFS for any concentration or thickness.

3.3.2 Sample geometry influence

In 2012 a work by Larsen, Thorkildsen and Nicholson [43] take care of one aspect never treated before, studying how the attenuating factors experimented during fluorescence EXAFS are influenced by the geometry of the sample.

In this work the starting point is again Eq.(3.6) now rewritten as:

$$I_f \propto I_0 \epsilon_X G \mu_X \mathcal{A} \tag{3.11}$$

where it is introduced ϵ_X as the fluorescence efficiency, G as a factor dependent to the geometry of the detector, omitted in this work. The last new term introduced is a geometry dependent dimensionless absorption factor defined as

$$\mathcal{A} = \mathcal{A}(\mu_t, \mu_f) = \frac{1}{V} \int_V \mathrm{d}v e^{-(\mu_t s_o + \mu_f s_h)} \tag{3.12}$$

with V the volume associated with the irradiated part of the homogeneous sample. s_o and s_h are path lengths along the respective directions of incidence and detection as shown in figure 3.6, the spherical case is

deduced with the same principles. $\mu_t = \mu(E)$ is the total linear absorption coefficient of the sample studied at incident energy, E, while $\mu_f = \mu(E_f)$ is at the fluorescence energy of the absorber E_f. $\mu_X(E)$ as introduced in previous chapters is the coefficient of absorption of the absorbing atom only.

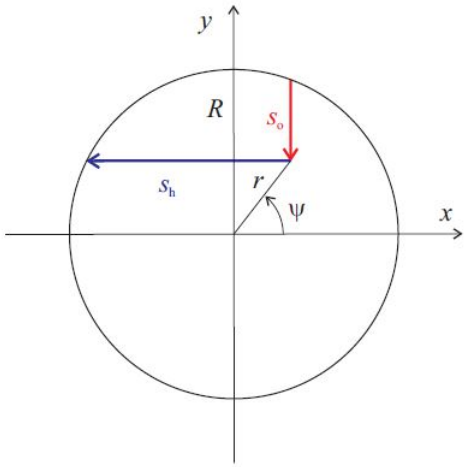

Figure 3.6: Sample with constant circular cross section of radius R. Path lengths along the direction of incidence and detection are s_o and s_h, respectively. These are oriented =90° with respect to each other. r and Ψ are the integrating variables.

The expression of the attenuation factor $\mathcal{A}$ is then derived for three different geometries (Fig. 3.7):

1. A laterally unlimited sample (slab):

$$\mathcal{A}_s = (\frac{1}{l_0})(\frac{1}{\mu_t + \mu_f \frac{\sin\phi}{\sin\theta}})(1 - \exp\left[-(\frac{\mu_t}{\sin\phi} + \frac{\mu_f}{\sin\theta})r\right])$$

This result, if properly rewritten is the same found in the previously cited works as [29, 36, 38].

2. Constant circular cross section (cylinder):

$$\mathcal{A}_c = \frac{1}{\pi}\int_0^1 \rho\,\mathrm{d}\rho \int_0^{2\pi} \mathrm{d}\psi e^{(-\Lambda_r[\sqrt{1-(\rho\cos\psi)^2}-\rho\sin\psi]+\mu_{ft}[\sqrt{1-(\rho\sin\psi)^2}+\rho\cos\psi])}$$

3. Varying circular cross section (sphere):

$$\mathcal{A}_s = \frac{3}{2\pi}\int_0^1 \mathrm{d}\zeta \int_0^{\sqrt{1-\zeta^2}} \rho\,\mathrm{d}\rho \int_0^{2\pi} \mathrm{d}\psi e^{\left(-\Lambda_r\left\{\left[\sqrt{1-\zeta^2-(\rho\cos\psi)^2}-\rho\sin\psi\right]+\mu_{ft}\left[\sqrt{1-\zeta^2-(\rho\sin\psi)^2}+\rho\cos\psi\right]\right\}\right)}$$

For the sphere and cylinder geometries it's not possible to have an analytical solution of the integral, thus it have to be evaluated numerically. It's also important to define the new dimensionless variable $\Lambda_r = \mu_t r$, where r is the radius of these objects, as it shows the dependency of the attenuation factors to the size of the sample. It also introduce in these formulas the relative absorption coefficient $\mu_{ft} = \frac{\mu_f}{\mu_t}$

The next step involves again the previously introduced 'averages assumption', it is thus defined:

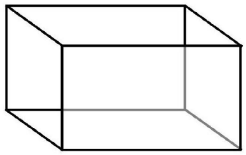

(a) Slab

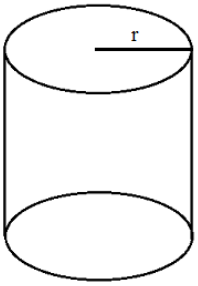

(b) Cylinder

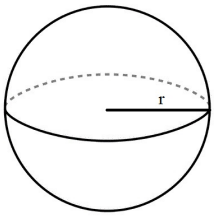

(c) Sphere

Figure 3.7: The three geometry models used to obtain their relative attenuation factors.

$\mu_x = \bar{\mu}_x(1+\chi)$

$I_f = \bar{I}_f(1+\chi_{exp})$

$\mu_t = \bar{\mu}_t + \bar{\mu}_x\chi$

$\mu_f = \bar{\mu}_f$

where the 'barred' quantities are result of proper averaging procedures.

It is now possible to derive the equation to determine the true EXAFS, χ, from the experimental measured EXAFS, χ_{exp} :

$$(1+\chi)\mathcal{A}(\bar{\mu}_t + \bar{\mu}_X\chi, \bar{\mu}_h) = (1+\chi_{exp})\mathcal{A}(\bar{\mu}_t, \bar{\mu}_h) \tag{3.13}$$

It is important to note that the correction is done directly to χ in the k-space.

First order correction - small sample limits

The need of software products for faster expression to evaluate the correction magnitude to be applied, inspired to considerate another assumption which was proven to be true for all the cases experienced in this work. In the limit of samples of small size, i.e $\mu_t r, \mu_f r << 1$, first order Taylor's expansion are used in Eqs.(3.12) and (3.13) to derive a simplified expression for the true EXAFS χ:

$$\chi = \chi_{exp}\left[1 + \bar{\mu}_X(\gamma r)(1+\chi_{exp})\right] \tag{3.14}$$

where γ is a geometrical factor defined such as:

Slab: $\gamma = \frac{\sqrt{2}}{2}$

Cylinder: $\gamma = \frac{8}{3\pi}$

Sphere: $\gamma = \frac{3}{4}$

The results for the sphere and the cylinder were initially found for cases where the detector is placed normal to the direction of the incident beam, however, I found it to be true for every detection position, if not considering the scattering effects introduced previously. This can be seen in Appendix B.

4

Experiment - Short Review

This chapter is focused on the experiments performed by the same diffraction team that published [43], in Grenoble, France. These were done to provide an experimental verification to the developed correction factors.

4.1 Experimental Details

4.1.1 Synchrotron

The Synchrotron is operating in 16 bunch mode, of the ESRF-SNBL (Swiss Norwegian Beam-lines) facility. The beamline setup is the SNBL-B, showed in Figure 4.1, included a Si (111) monochromator with mirrors and a homogeneous beam with rectangular cross section $h = 0.55\,\text{mm}$; $l = 2.2\,\text{mm}$. The detector used was a Si-drift detector (Vortex-EX S11 Nanotechnology), placed at an angle $\phi = 30°$ respective to the direction of the incoming beam. Room temperature: $20.5°C$.

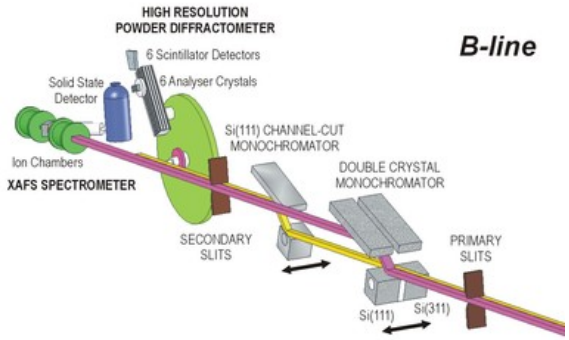

Figure 4.1: Schematic layout of the beamline. Figure is taken from ESRF official website.

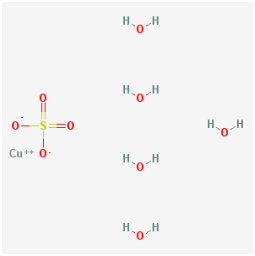

(a) 2D Structure

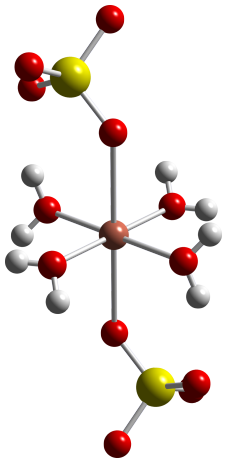

(b) 3D Structure

Figure 4.2: Structural models of the copper sulphate pentahydrate $CuSO_4 \cdot 5\,(H_2O)$. The absorbing element Cu has O as its first neighbor.

4.1.2 Samples

The material used to produce the samples was a commercially bought copper sulphate powder ($CuSO_4$). In Fig. 4.2 are represented the $3D$ and $2D$ Structures to show the absorber and its neighbors. It can be seen that in this compound, copper is surrounded by a tetragonally distorted octahedron of oxygen atoms and while the crystal structure assigned is triclinic leading to low symmetries [13, 24]. Previous EXAFS studies can be found in the work of Martens et al [17] and Joyner [18]. Since there was no interest on studying the slab model, two geometrical shapes were reproduced:

Cylinder

Liquid solutions of copper sulphate pentahydrate $CuSO_4 \cdot 5\,(H_2O)$ placed in thin-walled glass capillaries. 14 data sets were collected varying the concentration of the solution and the inner radius of the capillary. Details of the parameters are shown in Table 4.1.

Fluorescence absorption spectra was also measured for the glass capillaries of each inner radius. Figure 4.3 shows a comparison of the absorption spectra of the glass capillary and the total sample. However this was not used in this work as the Athena software, as shown in Figure 4.4 has implemented already good and accurate routines to remove the background effects such as the absorption of the sample containers. Thus the subtraction of the total and glass only absorption spectra would have accumulated more unnecessary noise error.

Figure 4.3 is also useful to introduce a technical issue experienced in EXAFS absorption measurements for most of the capillary samples. This is a small sharp rise in the absorption coefficient that happens around 9700 eV. It is caused by a multiple beam scattering event in the monochromator occurring in that particular energy range, the result is a systematic enhancement that is seen in the scans. A deep description

Sample number	Concentration (M)	Radius (mm)	Repetitions
1	0.20	1.00	4
2	0.20	1.50	4
3	0.20	0.70	7
4	0.20	0.30	31
5	0.20	0.20	11
6	1.00	1.50	6
7	1.00	1.00	8
8	1.00	0.70	10
9	1.00	0.20	15
10	0.76	1.50	7
11	0.76	1.00	7
12	0.32	1.00	7
13	0.32	0.70	40
14	0.52	1.50	8
15	0.52	1.00	8

Table 4.1: Parameters used for the capillary sample. Uncertainties estimated on parameters are: $\delta C \sim \pm 0.01\,\mathrm{M}$, $\delta r \sim \pm 0.05\,\mathrm{mm}$.

on how these "glitches" are formed and a model to minimize them can be found in the work of Boyce et al. [28]. However such a treatment goes beyond the purpose of this work and these were not implemented. An alternative easier way to deal with it that was considered, was to use a "deglitching" tool implemented in Athena, consisting in removing the "glitched points", however it was neglected as it sensibly modified the calculation of the EXAFS function $\chi(E)$. Therefore the glitch was kept in consideration but left inaltered as it wouldn't influence much the corrections to be successively performed.

Sphere

Due to the complexities of reproducing accurate spherical samples ensembles only one data set was measured, of a crystalline solid copper sulphate of radius $r = 0.45\,\mathrm{mm}$. The shape was given by a custom made air driven Bond-mill [26].

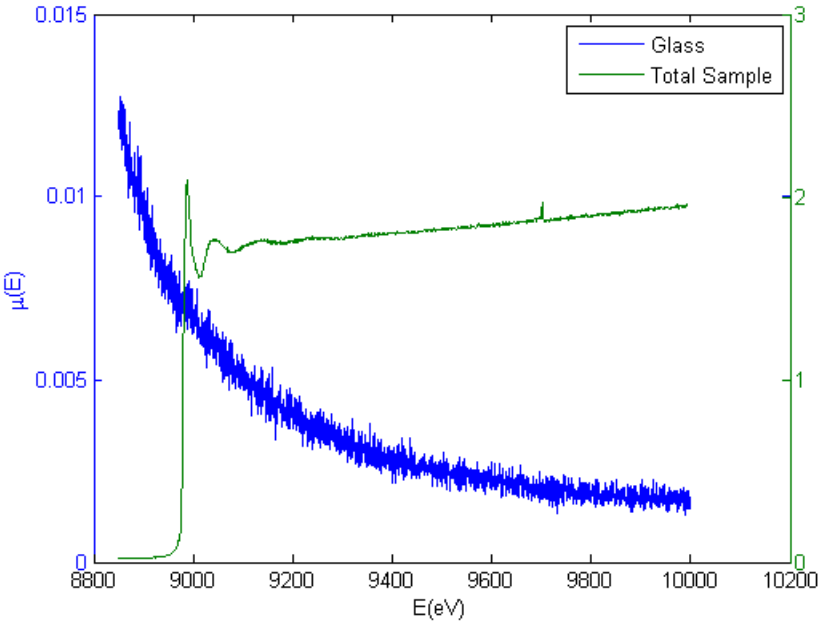

Figure 4.3: A plot of the absorption coefficient spectra before normalization, $\mu(E)$, of the empty glass capillary of 1mm radius (blue line) and the same filled with the sample (green line). The influence of the glass absorption is minimal, specially after the absorption edge and in the extended range making it an irrelevant source of attenuation. Note the different scales o the ordinate axes of the plots.

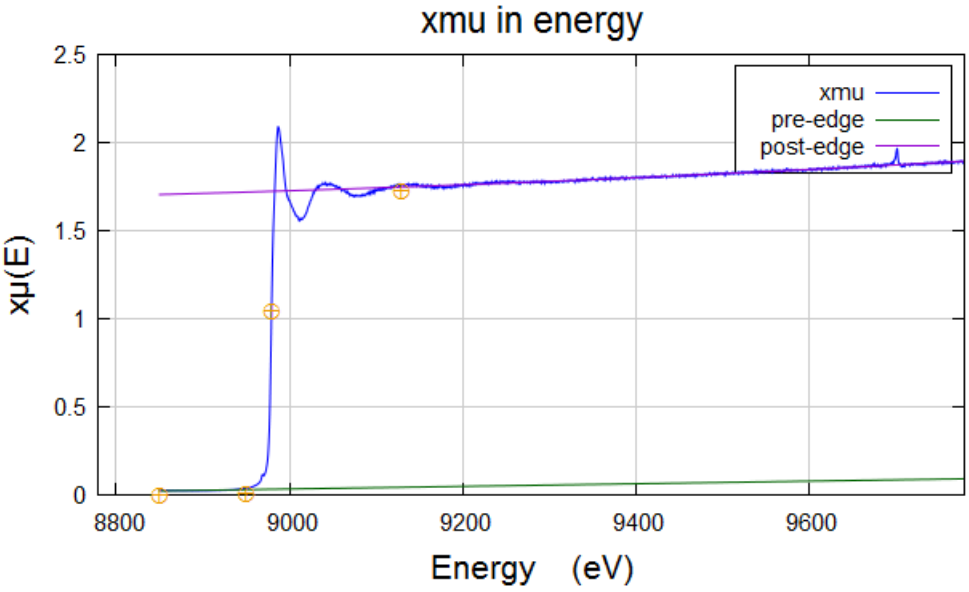

Figure 4.4: The green and purple lines, representing the pre- and post-edge lines respectively, besides being used to determine the absorption jump $\Delta\mu(E)$ to normalize the EXAFS in Eq.3.1 take care of the background absorption effects.

5

Data Processing and Analysis

5.1 Data processing and Analysis

The measured data was available as a *.txt* format file including all the relevant parameters and the measured values. By an adaptation involving an extraction and formatting of only the parameters of interests these could be imported in a software product dedicated to XAFS analysis, called Athena [39]. Here the absorption spectra $\mu_t(E)$ was obtained and normalized for every single repetiton of each data set.

The data analysis procedure (documented in figures of appendix C) successively involved the following steps:

1. Calibration: Every spectra was re-calibrated to the theoretical absorption edge of the absorbing atom (Cu) $E_0 = 8790\,\text{eV}$. This was done by shifting the peak in the plot of the first order derivative of the absorption coefficient to the theoretical value.. This was a crucial step in order to obtain accurate values of χ in k- and R-space.

2. Alineation: Every spectra of each data set was realigned to the new calibrated absorption edge in order to allow a further merging.

3. Merging: All the normalized absorption coefficient spectra of the same data set were merged in order to have only one spectrum for each parameter setting.

The software is then able to reproduce the background function of the absorbing atom μ_X to calculate the EXAFS function, $\chi(E)$, as in Eq. (3.1) and plot it in k- and R-space.

In Figures presented in appendix C, these steps are summarized. It can also be observed that the self-absorption effect affects the spectrums as one would expect. Both the absorption μ and the EXAFS χ are more attenuated as the size of the sample gets thicker, and amplified as the sample is more diluted.

In order to test the correction models developed previously the data was then exported in a ASCII *.txt* format file containing the following coordinates: E, μ_t, μ_X and $\chi(E)$.

5.2 Self-Absorption Correction

The corrections were then performed through a Mathematica [41] script (visible in Appendix C) both to the first order of approximation and to the full numerical evaluation according to Eqs. (3.14) and (3.13) respectively. The scripts return a ASCII *.datq* files containing columns data of the following quantities: k, E, μ_t, χ_{exp}, χ. This could then be re-imported in Athena as $\chi(k)$ data to simultaneously display multiple spectra and obtain the 'true' $\chi(R)$.

Figures (5.1, 5.2, 5.3, 5.4) in the next pages show the results of these correction. The EXAFS in k-space, $\chi(k)$, are k-weighted, $k\chi(k)$; while in R-space, $\chi(R)$, are k^2-weighted after the correction, and magnified on meaningful coordinates ranges, for a better display.

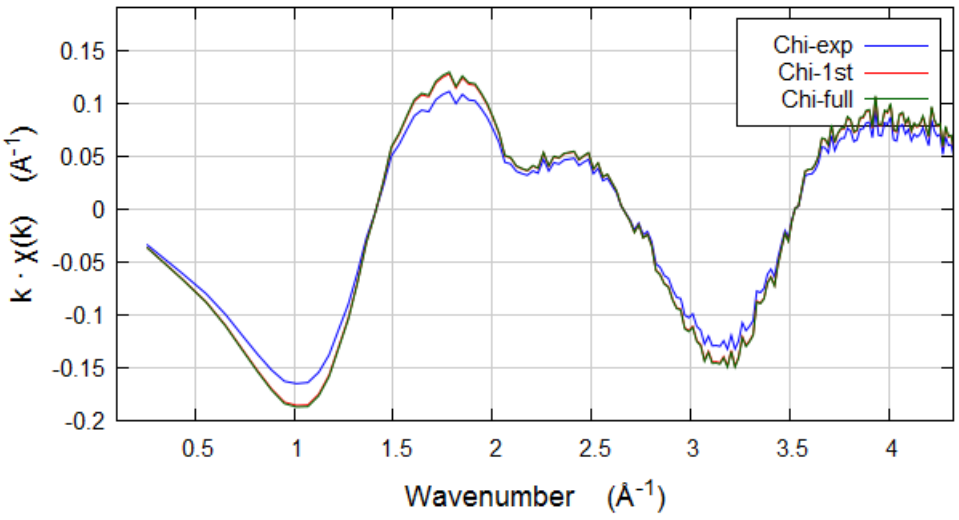

Figure 5.1: A plot of the $\chi(k)$ for the capillary sample n° 6. The blue line represent the measured EXAFS, $\chi_{exp}(k)$, while the red and green line represent the corrected EXAFS, $\chi(k)$, using the first order approximation in Eq.(3.14) and the full routine (3.13), respectively. The results are here are also k-weighted.

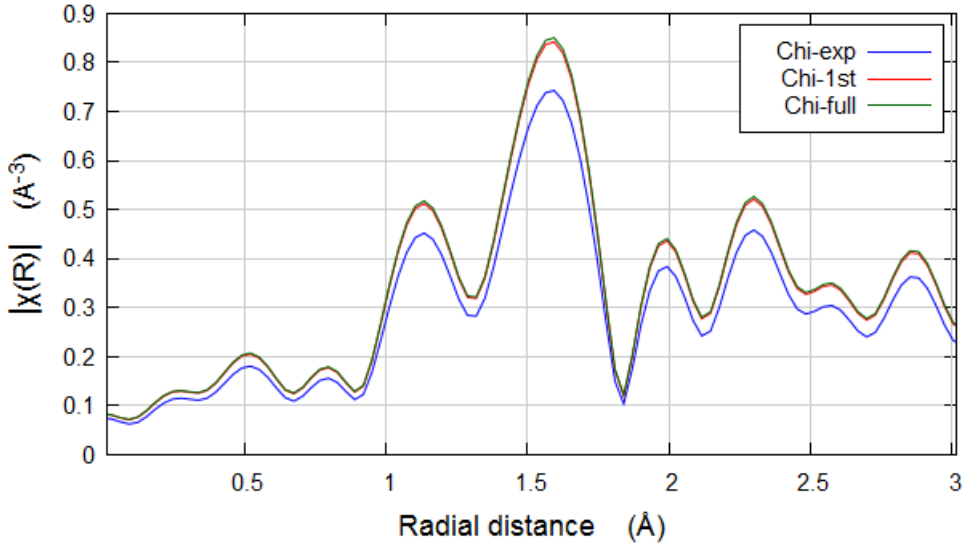

Figure 5.2: A plot of the $\chi(R)$ and corrected respectives, for the capillary sample n° 6.

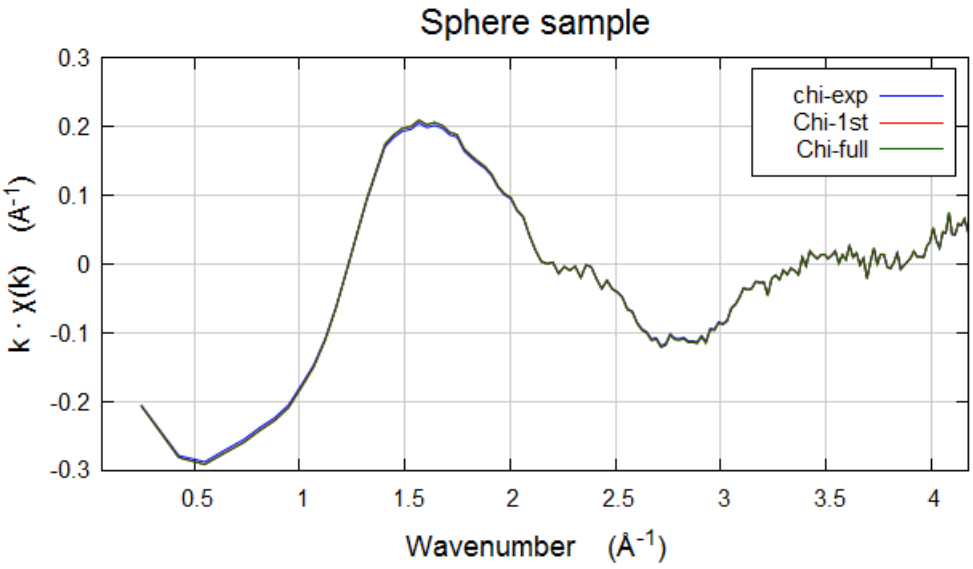

Figure 5.3: A plot of the $\chi(k)$ and corrected respectives, for the spherical sample.

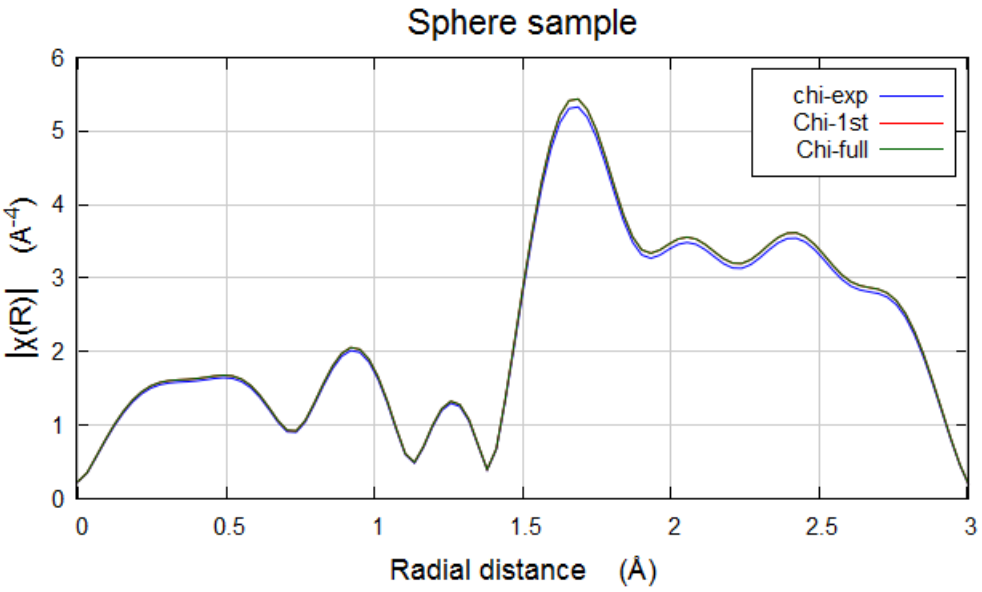

Figure 5.4: A plot of the $\chi(R)$ and corrected respectives, for the spherical sample.

Figure 5.5 shows the measured EXAFS of the spherical sample is corrected in first order approximation (3.14), with both cylindrical and spherical models, to make comparisons.

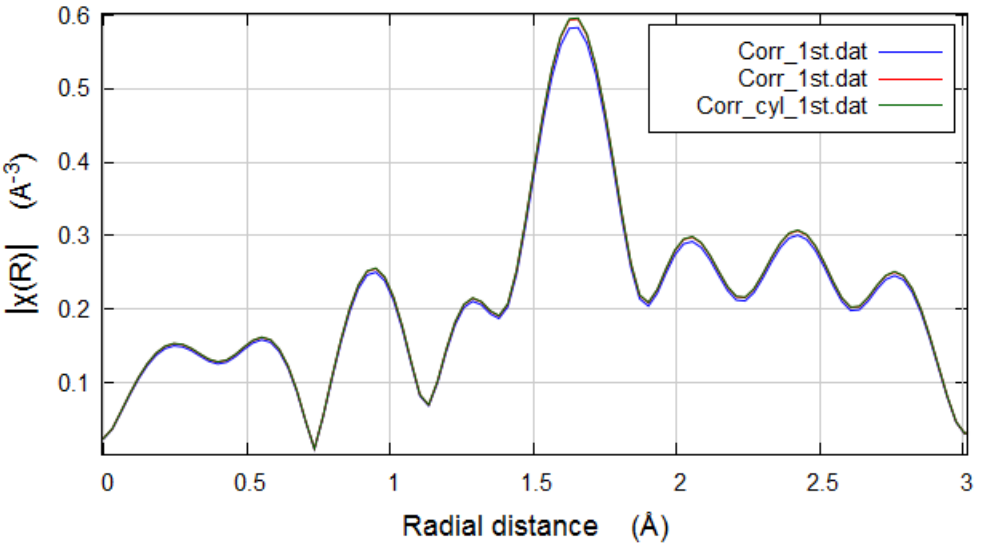

Figure 5.5: The spherical sample measured EXAFS (blue line), is now corrected with both the cylindrical and spherical correction models listed in Eq. (3.14) to denote the difference.

In figure 5.6 is also displayed in the second scale the relative oscillation gain by calculating:

$$\chi_{rel}(k) = \frac{|\chi(k) - \chi_{exp}(k)|}{\chi_{exp}(k)} \tag{5.1}$$

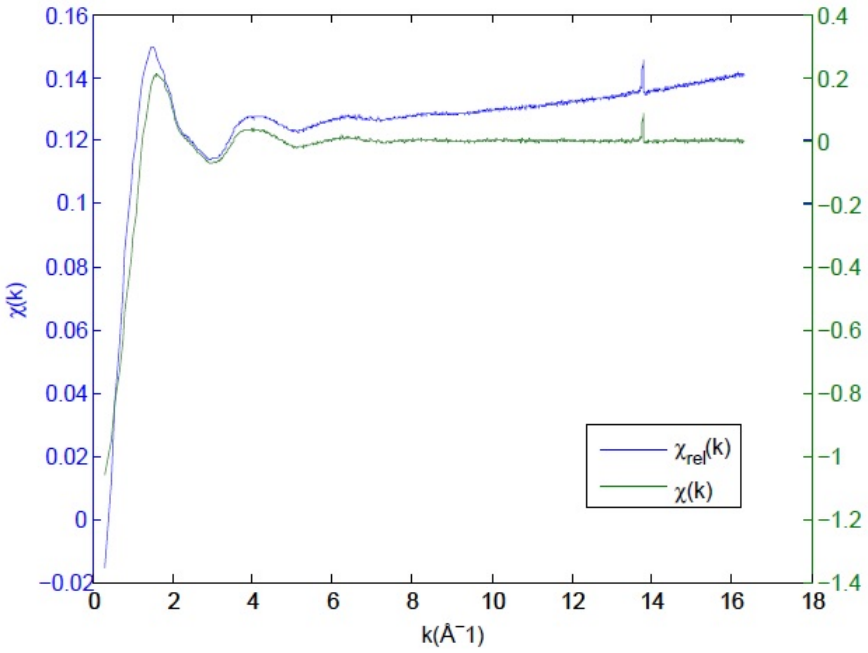

Figure 5.6: A plot of the relative (blue line) and corrected (green line) EXAFS, $\chi_{rel}(k)$ and $\chi(k)$ respectively.

The behavior of this function follows with high sensitivity the EXAFS function showing a proportional dependence on the correction to the measured $\chi(k)$. It is crescent in the long range according to the dependence on the background function μ_X, while the amplitude gain is caused by the dependence on the geometrical factor, γ, and thickness r. This relation was also used to analyze the influence of modifying the parameters in the corrections in figures (5.7, 5.8, 5.9 and 5.10). It is observed that the mean value of the relative EXAFS function, $\langle\chi_{rel}\rangle$[1], is crescent with both radius and concentration, seeming to be linear with radius increases, whereas increases with higher concentration values are more subject to systematic errors.

[1] A gaussian weighted average to better account when the function gets stable was considered, however for convenience the arithmetical average was used here.

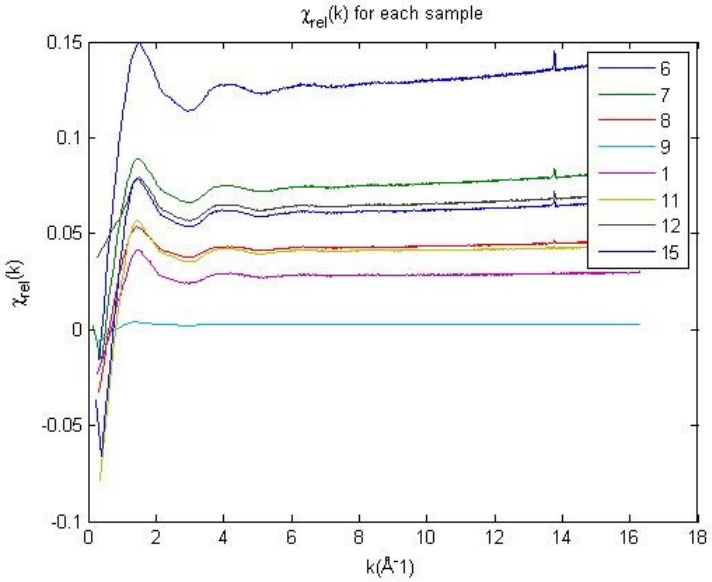

Figure 5.7: A plot of the $\chi_{rel}(k)$ defined in Eq. (5.1) for the samples used in figures 5.8 and 5.9. The numbering of the samples in legend is referring to 4.1.

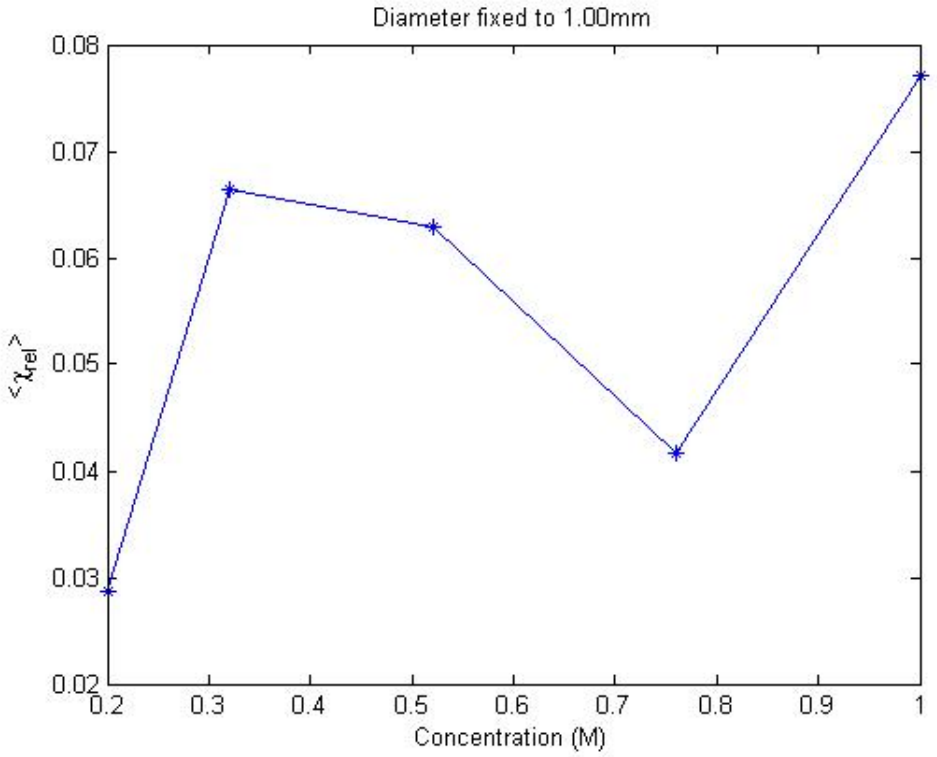

Figure 5.8: A plot of the arithmetical mean value of the relative EXAFS, $\langle\chi_{rel}\rangle$, for samples with fixed radius and varying concentration.

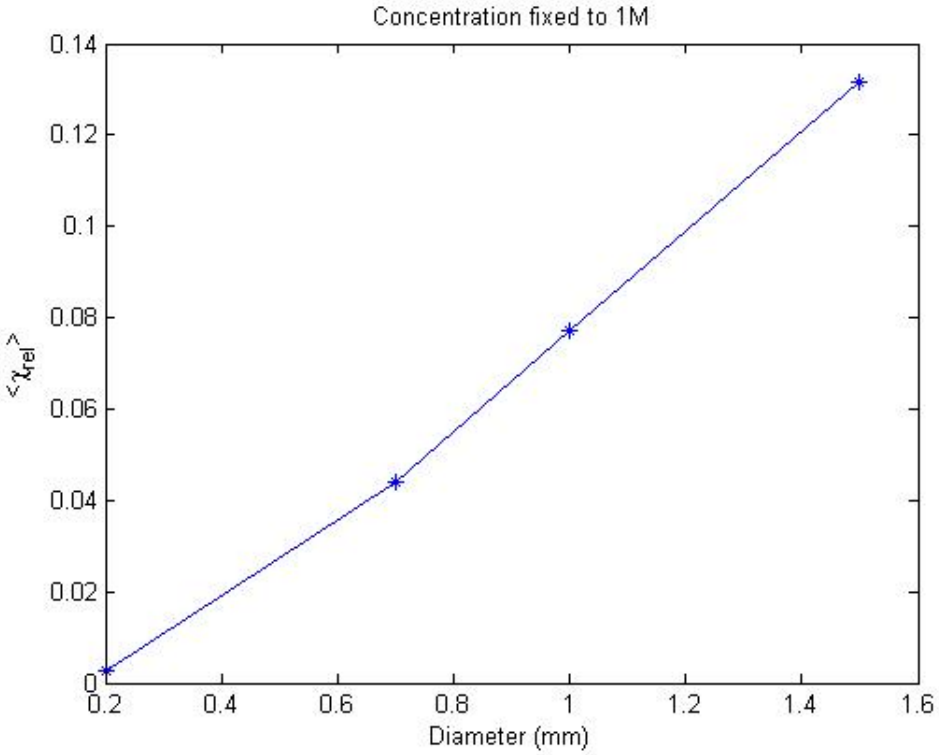

Figure 5.9: A plot of the arithmetical mean value of the relative EXAFS, $\langle \chi_{rel} \rangle$, for samples with fixed concentration and varying radius.

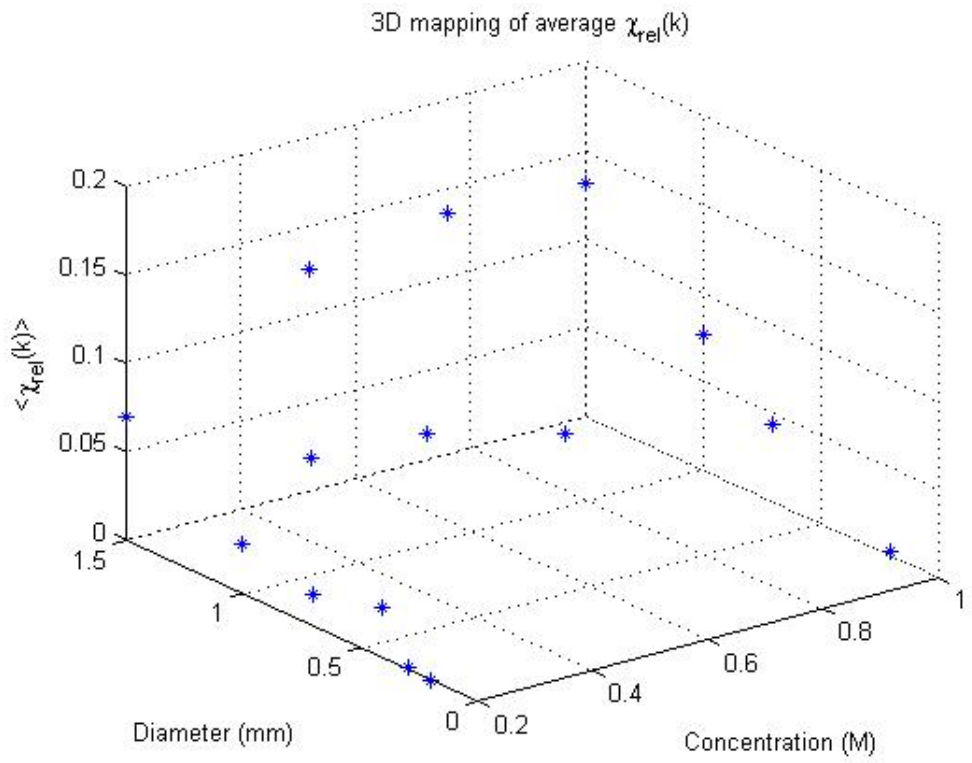

Figure 5.10: A 3-D plot mapping of all the cylindrical samples provided. $X - Y$ coordinates are representing the two parameters of inner radius and concentration, while Z height coordinate is the arithmetical mean value $\langle \chi_{rel} \rangle$.

6

Conclusion

In this chapter it will be discussed the results of the corrections and possible applications or extensions.

6.1 Results and discussion

A first result to be noted is that an EXAFS database for copper sulphate was obtained for liquid and solid state phases. This could be used in future tasks such as fits, or analyses in order to extract the structure parameters.

6.1.1 Effects of varying parameters

As predicted by the self-absorption models highlighted in chapter 3 an attenuation (or increase) of the absorption coefficient was noted by a variation of the concentration and inner radius parameters. The following report is carried by keeping one of these parameters fixed and changing the other.

Varying inner radius

As it was already shown in figure 3.4, the absorption spectra is attenuated as the inner radius is increased. By taking the thinnest sample as reference (denoted with 'ref' subscript) an amplitude relative reduction, A_r, was obtained by the relation:

$$A_r(E) = \frac{|\mu(E) - \mu_{ref}(E)|}{\mu_{ref}(E)} \tag{6.1}$$

Figure 6.1 shows a plot of $A_r(E)$ against energy E, for samples of different size.

Varying concentration

Figure 6.2 shows instead how the absorption spectra is attenuated by diluting the sample. A_r was obtained as in eq. 6.1 by taking now the most diluted as reference, and plotted in figure 6.3 as well.

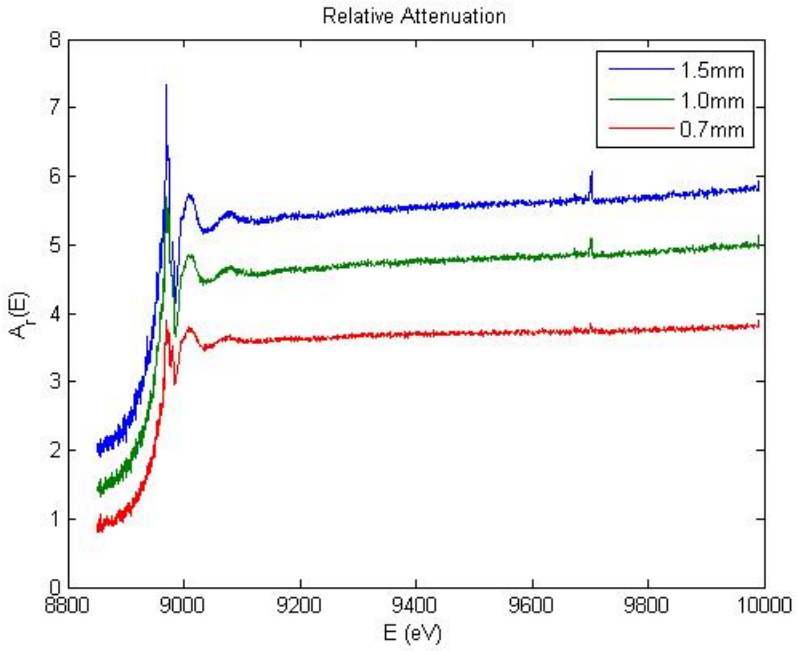

Figure 6.1: A plot of the relative amplitude reduction, $A_r(E)$. The sample used as reference has radius $r = 0.01\,\text{cm}$, while the colored lines (red, blue and green) reflect how much the absorption is attenuated as the radius increases to $r = 0.035\,\text{cm}$, $r = 0.05\,\text{cm}$ and $r = 0.075\,\text{cm}$.

It can be noted that both parameter variations exhibit the self-absorption effect and the same result is found when considering instead the EXAFS function, χ, in both k- and R- space [1]. By taking a look to the values of $A_r(E)$ in figures 6.3 it is also clear that the correction gain scales faster with increases of inner radius rather than concentration.

6.1.2 Influence of corrections

From an analysis of the corrections[2] performed for every different sample it can be observed that:

- As expected the correction routines don't shift the peaks of the $\chi(R)$, meaning that it doesn't change the determination of the interatomic distance, R, between the absorber (Cu) and the first neighbor (O). What is modulated is the amplitude of the oscillations $\chi(k)$ and thus of $\chi(R)$. This reflects in changes in the extrapolation of other relevant chemical properties such as the coordination number, the Debye-Waller factor etc...[3]

- Another aspect that it can be seen is that the correction amplification is highly sensible to the thickness parameter r, while changes in concentration parameter M don't have such strong impact on the corrections.

[1] However results are not shown here to avoid redundancy.
[2] This was done mainly by comparisons between the $\chi_{rel}(k)$ of each sample.
[3] These were not extracted in this work as it would have required much more time in the comprehension of another software, Artemis [39], of the same developer of Athena. Therefore this is a plausible prediction without any number to support it.

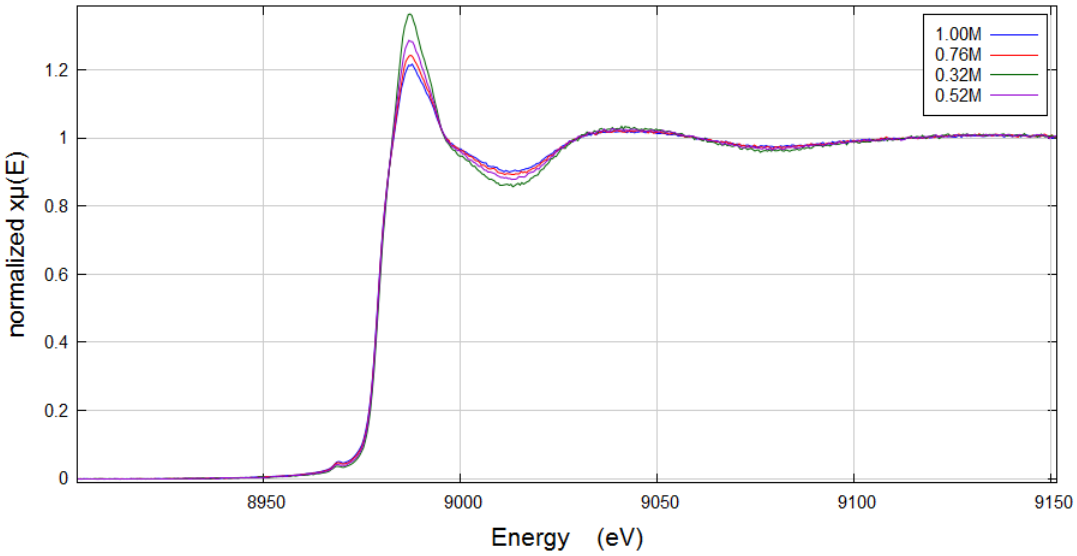

Figure 6.2: A plot of the normalized absorption coefficient $\mu(E)$ obtained by multiple concentration values.

- A comparison between the correction amplitude for the spherical and the cylindrical case, in Fig. 5.5, denotes that the different geometry of the sample doesn't play a role important as the thickness r for the thin samples, but it's expected to be more relevant for thicker samples.

- To state the advantage of using this new method of correction accounting for the geometry of the sample, it is shown in figure 6.4 a comparison by applying both the cylindrical and slab[4] correction models to the measured exafs $\chi(k)$. It is found for the example in figure an amplitude gain of $\langle A_r \rangle = 0.0204$[5]. Thereby there is a clear advantage of using these correction models in case of special geometris of the sample.

6.2 An eventual refinement

In all the work involving the correction to the self-absorption effect, one important aspect was the choice of the $\mu_X(E)$ parameter to be implemented in the routines. As a reminder, it is theoretically the absorption coefficient (in cm^{-1} unit) of the absorbing element, copper in this case. This work relied on an important assumption, that is the background function μ_{bkg} retrieved from Athena software would match it good enough.

A more accurate procedure would have been to use instead for $\mu_X(E)$ tabulated data for the absorption coefficient of copper, taken from well proven database such as XCOM [40] or FFAST [30, 37]. However Athena software treats measured μ as a dimensionless value, resulting in the requirement of its conversion to the cm^{-1} unit. That means converting the measured values used for EXAFS analysis (i.e. readings from

[4]It is important here to stress that all the previous correction models were developed for the slab geometry of the sample.
[5]This is calculated with the same procedures shown in eq. (6.1) and section 5.2

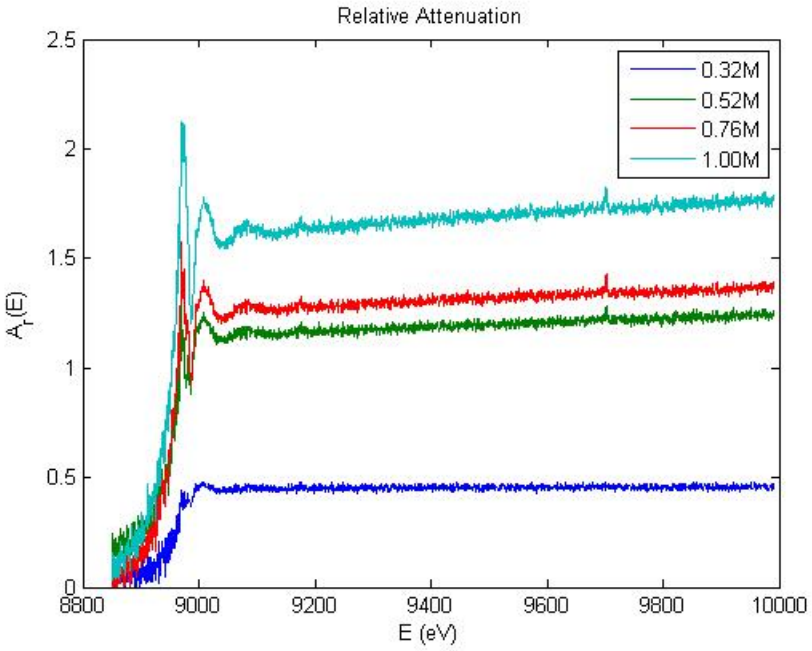

Figure 6.3: A plot of the relative amplitude reduction, $A_r(E)$. The sample used as reference has concentration $M = 0.20\,\mathrm{M}$, while the colored lines (blue, green, red and teal) reflect how much the absorption is attenuated as the radius increases to $M = 0.32\,\mathrm{M}$, $M = 0.52\,\mathrm{M}$, $M = 0.76\,\mathrm{M}$ and $M = 1.00\,\mathrm{M}$.

ion chambers) into actual X-Ray intensities, and try to account for anything else in the beam path that could eventually attenuate the X-Rays. If the measurement regime is in transmission, this can be relatively easily performed. In fluorescence regime, that is the case of this work, this process would require a very accurate measure of the solid angle Ω of the detector, the fluorescence efficiency ϵ_X, and the attenuation of the fluorescence reaching the detector from the sample. This makes it a complicate process to do post facto, specially because it wasn't the actual point of the experiment.[6]

6.3 Looking further

The rise of a new self-absorption correction model according to the geometrical shape of the sample allows to refine the future fluorescence EXAFS measurements for thick samples that cannot be reproduced in ideal shapes (as the slab). One example of this is the recent (2015) work of Bera and Antonio [44] where the EXAFS study of trivalent cations is carried for a sample represented by an inverted pendant drop (spherically modeled).

The same procedure could be applied to new geometrical shapes according to the experimental needs. The first order approximation, specially, can be implemented in the XAFS analysis software products, as it returns a meaningful and relative rapid correction by the bare input of the sample thickness (expressed in

[6] For these useful information I must thank Matt Newville and Christopher Thomas Chantler for the mail exchanges through the Ifeffit mailing list.

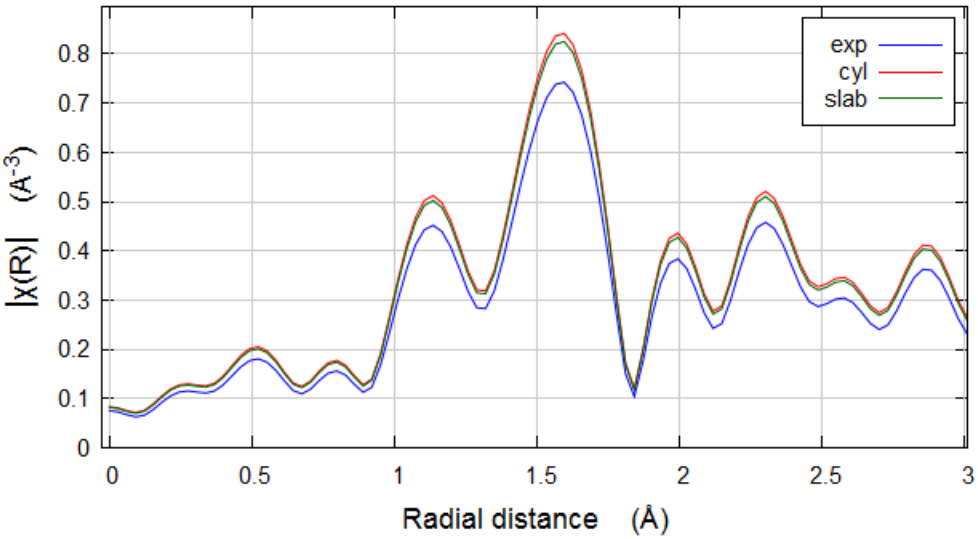

Figure 6.4: A plot of the $\chi(R)$ for the sample n° 10. The blue line represent the measured EXAFS function, while the red and green lines are respectively the corrected EXAFS function using the cylinder and slab models.

cm unit), and the geometrical model. The full routine, alternatively provides a slower[7] correction that can be applied when higher precision is required.

[7]From my laptop of an old generation, it was an approximately 30 minutes routine, however I expect to be in the minutes order in faster computers.

Appendix A

Chemical Properties from EXAFS

This appendix will describe the meaning of the chemical properties possibly extrapolated from EXAFS. As it is mentioned in Chapter 3 it is an atomic probe to determine the atomic structure of samples studied by meaning of the following terms: coordination number N, interatomic distance R, Debye Waller factor $e^{-2k^2\sigma^2}$. This is done by the use of Eq. 3.3 reported again for convenience

$$\chi(k) = \sum_j \frac{N_j e^{-2k^2\sigma_j^2} f_j(k)}{kR_j^2} \sin\left[2kR_j + \delta_j(k)\right]$$

by knowing the scattering amplitude $f(k)$, and phase shifts $\delta(k)$. These can by obtained by knowing the chemical structure[1] of the compound observed.

A.1 Coordination number N

In condensed matter descriptions, the coordination number of a central atom (in EXAFS case the X-Ray absorber) in a molecular or crystalline system reflects the number of its nearest neighbors. In simple chemistry this number is equal to the count of the other atoms bonded to the central one.

However in solid-state structures of crystals the bonds are often not clearly defined, making this a non trivial quantity. In order to be determined, the crystal structure has to be found first.

An interesting related work is the one of Eidsness and Elder [23], where the gold coordination number with sulfur and phosphorus ligands examination is carried trough EXAFS analysis of metabolites containing gold.

[1] It is also possible to start from a initial simple structure and fit from the parameters obtained this way.

A.2 Debye-Waller Factor

In condensed matter physics, the Debye-Waller factor is used to describe the attenuation of X-Ray scattering or coherent neutron scattering caused by thermal motion. For XAFS it describes instead the attenuation of $\chi(k)$ due to the thermal and static disorder in the bond length.

In the simplified EXAFS equation 3.3:

$$\chi(k) = \sum_j \frac{N_j \, e^{-2k^2\sigma_j^2} f_j(k)}{kR_j^2} \sin\left[2kR_j + \delta_j(k)\right]$$

is represented by the highlighted exponential term:

$$e^{-2k^2\sigma_j^2}$$

thus it's dependent on the scattering vector, $\vec{k}$. The σ^2 term, with the subscript j cutted for convenience, receives two contributions:

$$\sigma^2 = \sigma_T^2 + \sigma_S^2 \tag{A.1}$$

σ_T^2 is the thermal contribution, related to σ, the root mean square displacement of the neighboring atom with respect to the absorber, by $\sigma_T^2 = 2\sigma^2$. σ_S^2 reflects any static disorder present in the shell of N atoms, and is related to the static displacement of the i-th atom from the average shell distance, ΔR_l, by $\sigma_S^2 = N^{-}1 \sum_{l=1}^{N} \Delta R_l^2$. How these results are obtained can be retrieved in the works [16, 18, 16]. The study of Copper Sulphate Pentahydrate of Joyner [18] provides also a good example on how these parameters are extrapolated from an EXAFS measurement. Another good example is the more recent work of Dalba in 1997 [32] that considerates the Einstein model aswell.

A.3 Interatomic Distance R

The interatomic distance between the absorbing element and the first j-shell of neighbors, R_j, is found in EXAFS studies by using the mathematical tool of the Fourier Transform. As seen in eq. (3.3), each shell of atoms contributes with a sin function multiplied by a slowly varying amplitude function, therefore a Fourier transform of data of k-weighted $\chi(k)$ with respect to $e^{-i(2kr+\delta_j(k))}$ will have a peak at $r = R_j$.

Usually the Fourier transform is taken leaving out the phase shift $\delta_j(k)$ to make it easier. In this way each peak will result shifted by an amount $\delta_j'(k')$, that reflects a proper average over the first derivative of $\delta_j(k)$.

A seen in figures (5.2, 5.4) the $\chi(R)$ has a peak around the value of $R = 1.60$ Åreflecting the Cu−O bond distance between the copper atom and the first neighboring shell of oxygen atoms. This is in accord with the results of Joyner [18] and Martens.

Appendix B

Detection geometry influence

This appendix takes care of one aspect to be considered in order to fulfill the requirements for the for the first order approximation of the corrections. In the literature used to obtain the correction routines [43], to simplify things the detection geometry was assumed to be so that θ and ϕ, the incident and exit angle of the radiation on the sample satisfied $\theta + \phi = 90°$. This because of two main reasons.

First of all in fluorescence experiments the generated X-Ray wave is emitted isotropically, so by placing the detector normal to the source the scattering contributions are eliminated.

Secondarily in the first order approximation used to find the attenuated factors summarized in (3.14), it was assumed a 90° detection geometry.

However the measurements analyzed in this report have been done with a geometrical setup of the detector placed at 30° with respect to the source. Therefore the following Mathematica script studies how the $\langle s_h \rangle$ and $\langle s_o \rangle$, defined in figure 3.6, are modified for different detection angles.

(a) Cylinder

(b) Sphere

Figure B.1: A plot of the volume average fluorescence path length $< s_h >_V$ as a function of the detection angle ϕ.

```
pc[β_]:=
1/Pi*
NIntegrate[ρ*(Sqrt[1-(ρ*Sin[(Pi/2)-β+θ])^2]+(ρ*Cos[(Pi/2)-β+θ])),
{ρ,0,1},{θ,0,2*Pi}]
checkcyl=Table[{Pi/10*i,pc[Pi/10*i]},{i,0,20}];
plotcyl=ListPlot[checkcyl,AxesLabel→{"β",""},Joined→True]
ps[β_]:=
3/(2*Pi)*
NIntegrate[
ρ*(Sqrt[1-ζ^2-(ρ*Sin[(Pi/2)-β+θ])^2]+(ρ*Cos[(Pi/2)-β+θ])),
{ζ,0,1},{ρ,0,Sqrt[1-ζ^2]},{θ,0,2*Pi}]
checksp=Table[{Pi/10*i,ps[Pi/10*i]},{i,0,20}];
plotsp=ListPlot[checksp,AxesLabel→{"β",""},Joined→True]
```

The results shown in Figure B.1 shows that the first order approximation has no dependency on the detection geometry for the sphere, and nearly no dependency for the cylinder.

Appendix C

Software documentation

In this appendix there will be shown a brief documentation on how Athena works in the analysis phase, and the Mathematica scripts used in the correction.

C.1 Athena

For the sake of the eventual curiosity of the reader a few screen-shots and an introductory explanation on how Athena works in the first stage will be reported.

Importing data

Data can be imported as $\mu(E)$ or $\chi(k)$. Energy column (in E or k space) must be defined as abscissa, while ordinate can be defined as a single column by selecting it as numerator, or as a ratio by combining multiple columns as numerator and denominators.

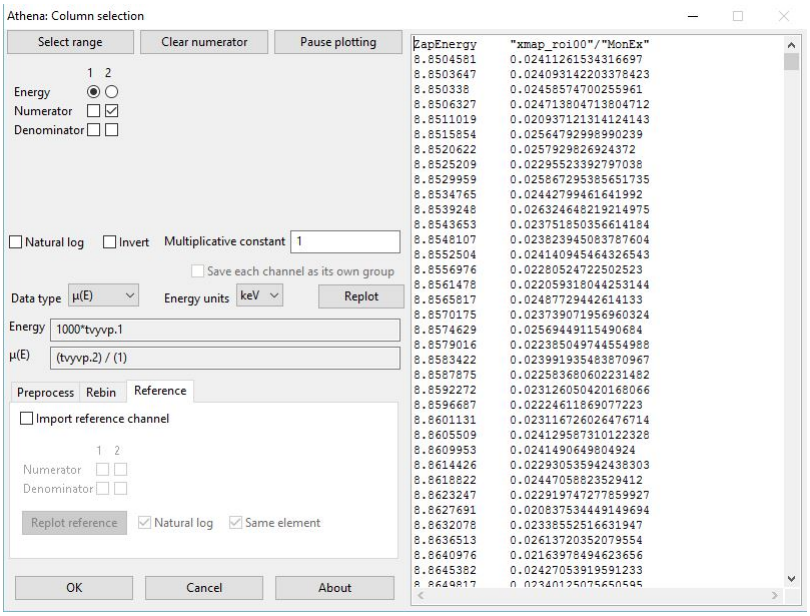

Figure C.1: The importing screen of the Athena software.

Calibration and Alineation

The absorption edge is calibrated by picking the maximum in the derivative plot of the absorption coefficient (Fig. C.2, for more accuracy the software also allows to shift the nearest zero point in the second derivative. This stage can also provide a plot preview of the data that is going to be imported.

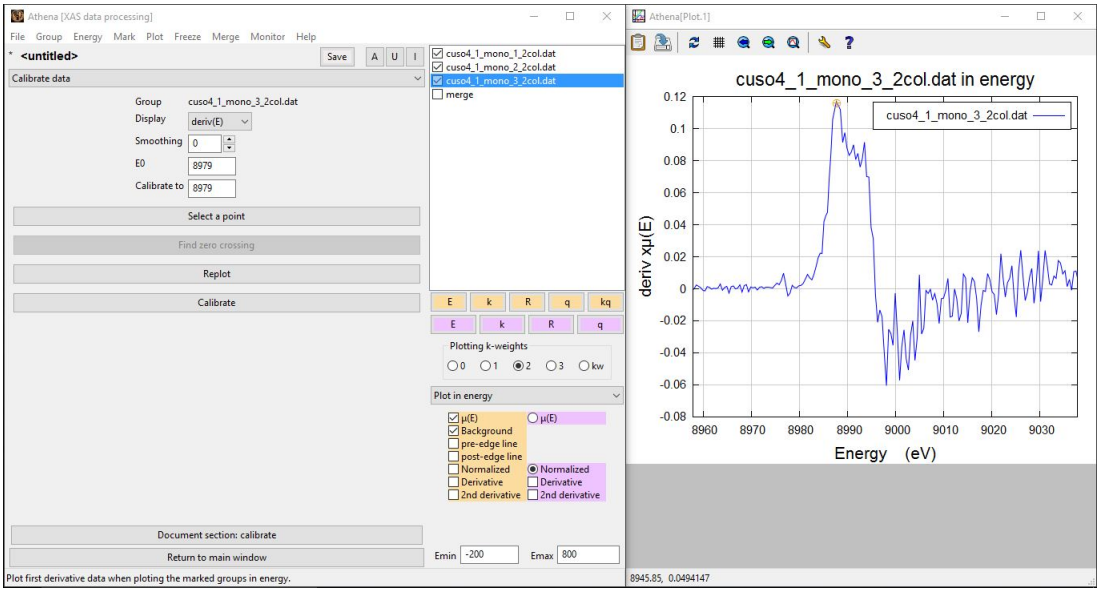

Figure C.2: Calibration screen.

The alineation is then performed by aligning all the data set to the previously calibrated one (Fig. C.3). Only at this point the theoretical absorption edge should be set for all the data sets.

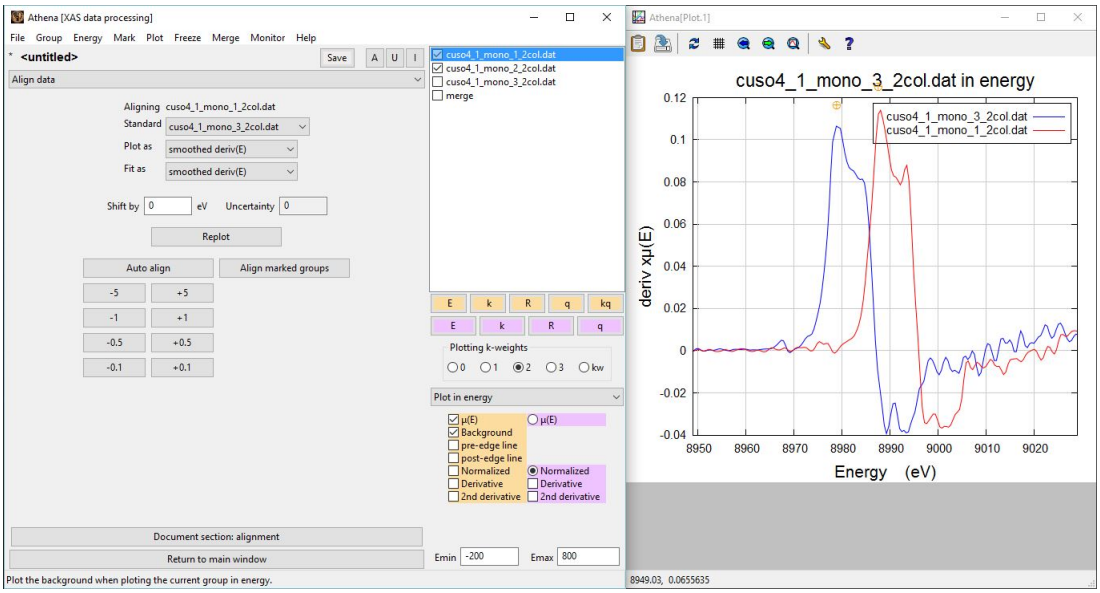

Figure C.3: Aligning screen.

Merging and plotting

Now it is possible to merge data sets and plot the result in the convenient space and quantity (Fig. C.4).

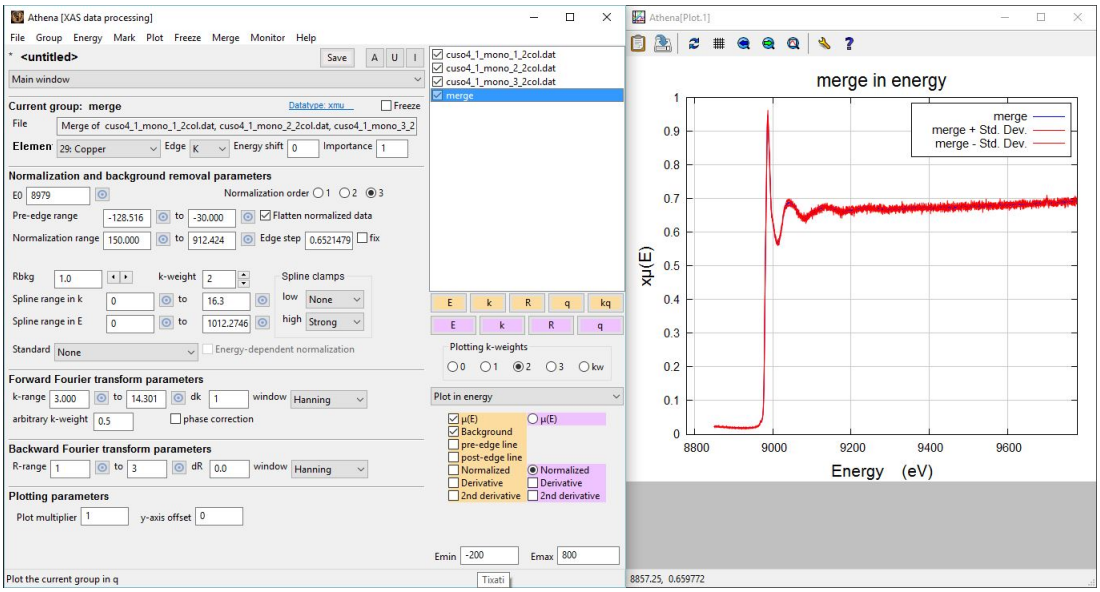

Figure C.4: The geometrical model used to obtain Eq. (3.7).

C.2 Mathematica scripts

Both scripts were adapted on the way the data as retrieved and organized, i.e. in folders with same title except for a number regarding to the number of the sample measured. They were also adapted to export

data in a way such that it could be easily imported in Athena [39].

In these cases the correction is for the cylinder case but it can be easily adapted to the sphere case by replacing $\zeta = \frac{8}{3\pi} r$ with $\zeta = \frac{3}{4} r$.

C.2.1 First order approximation

```
r =′ input′;
samplenr =′ input′;
ζ = (8/(3 ∗ Pi)) ∗ r;
κ[κe_, μ_]:=κe ∗ (1 + μ ∗ ζ ∗ (1 + κe))
data =
Import[
"C:\\Users\\Matteo\\Dropbox\\MASTER THESIS\\CuSO4
Data\\Capillary\\Raw Data\\cuso4_" <> ToString[samplenr] <>
"\\Final\\merge.dat"];
en = data[[All, 1]];
κe = data[[All, 8]];
μp = data[[All, 3]];
κr = ConstantArray[0, Length[data]];
κc = ConstantArray[0, Length[data]];
k = ConstantArray[0, Length[data]];
For[i = 1, i < (Length[data] + 1), i++,
κc[[i]] = κ[κe[[i]], μp[[i]]];
κr[[i]] = (κc[[i]] − κe[[i]])/κc[[i]];
k[[i]] = Sqrt[0.262468 ∗ (en[[i]] − 8979)];
]
compact = Transpose[{k, en, μp, κe, κc}]//TableForm;
Show[ListPlot[κc, PlotStyle → Blue], ListPlot[κe, PlotStyle → Red]]
ListPlot[κr, PlotStyle → Red]
Export[
"C:\\Users\\Matteo\\Dropbox\\MASTER THESIS\\CuSO4 Data\\Capillary\\Raw
Data\\cuso4_" <> ToString[samplenr] <> "\\Final\\Corr_1st.dat",
compact];
```

C.2.2 Full numerical evaluation

```
samplenr =′ input′;
r =′ input′;
ζ = (8/(3 * Pi)) * r;
Acyl[Λ_?NumericQ, μ_?NumericQ, μχ_?NumericQ, χ_?NumericQ]:=
1/Pi*
NIntegrate[
ρ*
Exp[
−Λ ((1 + μχ * χ) * (√(1 − (ρ * Cos[θ])^2) − (ρ * Sin[θ])) +
 μ (√(1 − (ρ * Sin[θ])^2) + (ρ * Cos[θ])))] , {ρ, 0, 1}, {θ, 0, 2 * Pi}]
ϰ[ϰe_, μ_]:=ϰe * (1 + μ * ζ * (1 + ϰe))
data =
Import[
"C:\\Users\\Matteo\\Dropbox\\MASTER THESIS\\CuSO4 Data\\Capillary\\Raw
Data\\cuso4_" <> ToString[samplenr] <> "\\Final\\merge.dat"];
en = data[[All, 1]];
ϰe = data[[All, 8]];
μo = data[[All, 2]];
μp = data[[All, 3]];
ϰr = ConstantArray[0, Length[data]];
ϰc = ConstantArray[0, Length[data]];
k = ConstantArray[0, Length[data]];
For[i = 1, i < (Length[data] + 1), i++,
chicyl[χexp_]:=
χ/.FindRoot[(1 + χ) * Acyl[r * μo[[i]], μo[[1]]/μo[[i]], μp[[i]]/μo[[i]], χ] ==
Acyl[r * μo[[i]], μo[[1]]/μo[[i]], μp[[i]]/μo[[i]], 0] * (1 + χexp), {χ, 2}];
ϰc[[i]] = chicyl[data[[i, 8]]];
ϰr[[i]] = (ϰc[[i]] − ϰe[[i]])/ϰc[[i]];
k[[i]] = Sqrt[0.262468 * (en[[i]] − 8979)];
]
```

```
compact = Transpose[{k, en, μo, ϰe, ϰc}]//TableForm;

Show[ListPlot[ϰc, PlotStyle → Blue], ListPlot[ϰe, PlotStyle → Red]]

ListPlot[ϰr, PlotStyle → Red]

Export[

"C:\\Users\\Matteo\\Dropbox\\MASTER THESIS\\CuSO4 Data\\Capillary\\Raw

Data\\cuso4_" <> ToString[samplenr] <> "\\Final\\Corr_full.dat",

compact]
```

Bibliography

The Bibliography used for the studies on this subjects is composed by three main books and releases, listed as 'Books'; and a collection of articles published by different authors, listed as 'Articles'.

It is also important to note that the theoretical description of the X-Ray Absorption process illustrated in Chapter 2, is necessarily largely inspired by the Elements of Modern X-Ray Physics [51] book and Handbook on Synchrotron Radiation [50].

All the figures instead are obtained through screen-shots or exporting of plots from software products, except for:

- Figures 2.1 and 3.2, re-adapted from book [51]
- Figure 2.2, taken from [52]
- Figure 3.1, taken from https://de.wikipedia.org/wiki/EXAFS-Spektroskopie
- Figure 3.5, taken from https://speakerdeck.com/bruceravel/understanding-self-absorption-in-fluorescence
- Figur 4.1, taken from http://www.esrf.eu/UsersAndScience/Experiments/CRG/BM01/bm01b
- Figures in 4.2, taken from https://pubchem.ncbi.nlm.nih.gov/compound/24463 and https://commons.wikimedia.org/wiki/File:Copper(II)-sulfate-pentahydrate-Cu1-coord-xtal-2007-CM-3D-balls.png

Articles

[1] Hugo Fricke. "The K-Characteristic Absorption Frequencies for the Chemical Elements Magnesium to Chromium". In: *Phys. Rev.* 16 (3 1920), pp. 202–215. DOI: 10.1103/PhysRev.16.202.

[2] G. Hertz. "über die Absorptionsgrenzen in derL-Serie". In: *Zeitschrift für Physik* 3.1 (1920), pp. 19–25. ISSN: 0044-3328. DOI: 10.1007/BF01356225.

[3] W. Kossel. "Zum Bau der Röntgenspektren". In: *Zeitschrift für Physik* 1.1 (1920), pp. 119–134. ISSN: 0044-3328. DOI: 10.1007/BF01881031.

[4] Axel E. Lindh. "Zur Kenntnis des Röntgenabsorptionsspektrums von Chlor". In: *Zeitschrift für Physik* 6.1 (1921), pp. 303–310. ISSN: 0044-3328. DOI: 10.1007/BF01327991.

[5] L. Meitner. "Über die Entstehung der β-Strahl-Spektren radioaktiver Substanzen". In: *Zeitschrift fur Physik* 9 (Dec. 1922), pp. 131–144. DOI: 10.1007/BF01326962.

[6] D. Coster. "Über die Absorptionsspektren im Röntgengebiet". In: *Zeitschrift für Physik* 25.1 (1924), pp. 83–98. ISSN: 0044-3328. DOI: 10.1007/BF01327511.

[7] Axel E. Lundh. "Über dieK-Röntgenabsorptionsspektra der Elemente Si, Ti, V, Cr, Mn und Fe". In: *Zeitschrift für Physik* 31.1 (1925), pp. 210–218. ISSN: 0044-3328. DOI: 10.1007/BF02980572.

[8] B. B. Ray. "Mehrfachabsorption und sekundäreK-Absorptionsgrenze im Röntgengebiet". In: *Zeitschrift für Physik* 55.2 (1929), pp. 119–126. ISSN: 0044-3328. DOI: 10.1007/BF01341219.

[9] Ben Kievit and George A. Lindsay. "Fine Structure in the X-Ray Absorption Spectra of the K Series of the Elements Calcium to Gallium". In: *Phys. Rev.* 36 (4 1930), pp. 648–664. DOI: 10.1103/PhysRev.36.648.

[10] M. Stobbe. "Zur Quantenmechanik photoelektrischer Prozesse". In: *Annalen der Physik* 399 (1930), pp. 661–715. DOI: 10.1002/andp.19303990604.

[11] J. D. Hanawalt. "The Dependence of X-ray Absorption Spectra upon Chemical and Physical State". In: *Phys. Rev.* 37 (6 1931), pp. 715–726. DOI: 10.1103/PhysRev.37.715.

[12] R. de L. Kronig. "Zur Theorie der Feinstruktur in den Röntgenabsorptionsspektren". In: *Zeitschrift für Physik* 70.5 (1931), pp. 317–323. ISSN: 0044-3328. DOI: 10.1007/BF01339581.

[13] G. E. Bacon and N. A. Curry. "The Water Molecules in $CuSO_4$. $5H_2O$". In: *Proceedings of the Royal Society of London A: Mathematical, Physical and Engineering Sciences* 266.1324 (1962), pp. 95–108. ISSN: 0080-4630. DOI: 10.1098/rspa.1962.0049.

[14] Leonid V. Azároff. "Theory of Extended Fine Structure of X-Ray Absorption Edges". In: *Rev. Mod. Phys.* 35 (4 1963), pp. 1012–1021. DOI: 10.1103/RevModPhys.35.1012.

[15] Edward A. Stern. "Theory of the extended x-ray-absorption fine structure". In: *Phys. Rev. B* 10 (8 1974), pp. 3027–3037. DOI: 10.1103/PhysRevB.10.3027.

[16] G. Beni and P. M. Platzman. "Temperature and polarization dependence of extended x-ray absorption fine-structure spectra". In: *Phys. Rev. B* 14 (4 1976), pp. 1514–1518. DOI: 10.1103/PhysRevB.14.1514.

[17] G. Martens et al. "Improved extended-x-ray-absorption fine-structure (EXAFS) studies applied to the investigation of Cu-O, Cu-N, and Cu-Br bond lengths". In: *Phys. Rev. B* 17 (4 1978), pp. 1481–1488. DOI: 10.1103/PhysRevB.17.1481.

[18] Richard W. Joyner. "An extended X-Ray absorption fine structure (exafs) study of copper (II) sulphate pentahydrate". In: *Chemical Physics Letters* 72.1 (1980), pp. 162 –164. ISSN: 0009-2614. DOI: 10.1016/0009-2614(80)80264-8.

[19] Edward A. Stern and Steve M. Heald. "An X-ray filter assembly for fluorescence EXAFS measurements". In: *Nuclear Instruments and Methods* 172.1 (1980), pp. 397 –399. ISSN: 0029-554X. DOI: 10.1016/0029-554X(80)90671-0.

[20] E. A. Stern. "EXAFS Spectroscopy: Techniques and Applications". In: (1981). Ed. by B. K. Teo and D. C. Joy, pp. 1–4. DOI: 10.1007/978-1-4757-1238-4_1.

[21] P.J. Durham, J.B. Pendry, and C.H. Hodges. "Calculation of X-ray absorption near-edge structure, XANES". In: *Computer Physics Communications* 25.2 (1982), pp. 193 –205. ISSN: 0010-4655. DOI: 10.1016/0010-4655(82)90035-2.

[22] Goulon. "On experimental attenuation factors of the amplitude of the EXAFS oscillations in absorption, reflectivity and luminescence measurements". In: *Journal de Physique* 43.3 (1982), pp. 539–548. DOI: 10.1051/jphys:01982004303053900.

[23] M. K. Eidsness and R. C. Elder. "EXAFS and Near Edge Structure III: Proceedings of an International Conference, Stanford, CA, July 16–20, 1984". In: (1984). Ed. by Keith O. Hodgson, Britt Hedman, and James E. Penner-Hahn, pp. 83–85. DOI: 10.1007/978-3-642-46522-2_24.

[24] C. A. Beevers and H. Lipson. "A brief history of Fourier methods in crystal-structure determination". In: *Australian Journal of Physics* 38 (1985), p. 263.

[25] S.P. Cramer et al. "A 13-element Ge detector for fluorescence EXAFS". In: *Nuclear Instruments and Methods in Physics Research Section A: Accelerators, Spectrometers, Detectors and Associated Equipment* 266.1 (1988), pp. 586 –591. ISSN: 0168-9002. DOI: 10.1016/0168-9002(88)90449-4.

[26] Alexander Nitkiewicz and S. Michael Sterner. "An improved Bond air mill for the preparation of spherical single crystals". In: 73.5-6 (1988), pp. 662–666. ISSN: 0003-004X. URL: http://ammin.geoscienceworld.org/content/73/5-6/662.

[27] Zhengquan Tan, Joseph I. Budnick, and Steve M. Heald. "Structural parameter determination in fluorescence EXAFS of concentrated samples". In: *Review of Scientific Instruments* 60.6 (1989), pp. 1021–1025. DOI: 10.1063/1.1140311.

[28] Frank Bridges, Xun Wang, and J.B. Boyce. "Minimizing "glitches" in XAFS data: A model for glitch formation". In: *Nuclear Instruments and Methods in Physics Research Section A: Accelerators, Spectrometers, Detectors and Associated Equipment* 307.2 (1991), pp. 316 –324. ISSN: 0168-9002. DOI: doi:10.1016/0168-9002(91)90199-Z.

[29] L. Tröger et al. "Full correction of the self-absorption in soft-fluorescence extended x-ray-absorption fine structure". In: *Phys. Rev. B* 46 (6 1992), pp. 3283–3289. DOI: 10.1103/PhysRevB.46.3283.

[30] C. T. Chantler. "Theoretical Form Factor, Attenuation, and Scattering Tabulation for Z=1-92 from E=1-10 eV to E=0.4-1.0 MeV". In: *Journal of Physical and Chemical Reference Data* 24.1 (1995), pp. 71–643. DOI: 10.1063/1.555974.

[31] Adriano Filipponi, Andrea Di Cicco, and Calogero Renzo Natoli. "X-ray-absorption spectroscopy and n -body distribution functions in condensed matter. I. Theory". In: *Phys. Rev. B* 52 (21 1995), pp. 15122–15134. DOI: 10.1103/PhysRevB.52.15122.

[32] G. Dalba and P. Fornasini. "EXAFS Debye–Waller Factor and Thermal Vibrations of Crystals". In: *Journal of Synchrotron Radiation* 4.4 (1997), pp. 243–255. DOI: 10.1107/S0909049597006900.

[33] Fran çois Farges, Gordon E. Brown, and J. J. Rehr. "Ti K-edge XANES studies of Ti coordination and disorder in oxide compounds: Comparison between theory and experiment". In: *Phys. Rev. B* 56 (4 1997), pp. 1809–1819. DOI: 10.1103/PhysRevB.56.1809.

[34] Robert C. Forrey, Jonathan W. Woo, and Kyeongjae Cho. "Model for Astrophysical X-Ray Absorption Fine Structure". In: *The Astrophysical Journal* 505.1 (1998), p. 236. URL: http://stacks.iop.org/0004-637X/505/i=1/a=236.

[35] P A Martin. "Multiple scattering and the Rehr-Albers-Fritzsche formula for the propagator matrix". In: *Journal of Physics A: Mathematical and General* 31.44 (1998), p. 8923. URL: http://stacks.iop.org/0305-4470/31/i=44/a=016.

[36] P. Pfalzer et al. "Elimination of self-absorption in fluorescence hard-x-ray absorption spectra". In: *Phys. Rev. B* 60 (13 1999), pp. 9335–9339. DOI: 10.1103/PhysRevB.60.9335.

[37] C. T. Chantler. "Detailed Tabulation of Atomic Form Factors, Photoelectric Absorption and Scattering Cross Section, and Mass Attenuation Coefficients in the Vicinity of Absorption Edges in the Soft X-Ray (Z=30–36, Z=60–89, E=0.1 keV–10 keV), Addressing Convergence Issues of Earlier Work". In: *Journal of Physical and Chemical Reference Data* 29.4 (2000), pp. 597–1056. DOI: 10.1063/1.1321055.

[38] C H Booth and F Bridges. "Improved self-absorption correction for fluorescence measurements of extended x-ray absorption fine-structure". In: *Physica Scripta* 2005.T115 (2005), p. 202. URL: http://stacks.iop.org/1402-4896/2005/i=T115/a=050.

[39] B. Ravel and M. Newville. "*ATHENA*, *ARTEMIS*, *HEPHAESTUS*: data analysis for X-ray absorption spectroscopy using *IFEFFIT*". In: *Journal of Synchrotron Radiation* 12.4 (2005), pp. 537–541. DOI: 10.1107/S0909049505012719.

[40] Hubbell J.H. Seltzer S.M. Chang J. Coursey J.S. Sukumar R. Zucker D.S. Berger M.J. and K. Olsen. "XCOM: Photon Cross Section Database (version 1.5)". In: (2010). URL: http://physics.nist.gov/xcom.

[41] Wolfram Research. "Mathematica 8.0". In: *Wolfram Research Inc.* (2010).

[42] M.L. Franquelo et al. "XRF, μ-XRD and μ-spectroscopic techniques for revealing the composition and structure of paint layers on polychrome sculptures after multiple restorations". In: *Talanta* 89 (2012), pp. 462 –469. ISSN: 0039-9140. DOI: 10.1016/j.talanta.2011.12.063.

[43] Helge B Larsen, Gunnar Thorkildsen, and David G Nicholson. "X-ray attenuation factors in fluorescence intensity emission—effects of finite sample size". In: *Physica Scripta* 86.6 (2012), p. 065601. URL: http://stacks.iop.org/1402-4896/86/i=6/a=065601.

[44] Mrinal K. Bera and Mark R. Antonio. "Polynuclear Speciation of Trivalent Cations near the Surface of an Electrolyte Solution". In: *Langmuir* 31.19 (2015). PMID: 25909822, pp. 5432–5439. DOI: 10.1021/acs.langmuir.5b01354.

[45] S.M.P. Kalaiselvi et al. "X-ray lithography of {SU8} photoresist using fast miniature plasma focus device and its characterization using {FTIR} spectroscopy". In: *Physics Letters A* 379.6 (2015), pp. 560 –569. ISSN: 0375-9601. DOI: 10.1016/j.physleta.2014.12.007.

[46] T. Hurma and S. Kose. "{XRD} Raman analysis and optical properties of CuS nanostructured film". In: *Optik - International Journal for Light and Electron Optics* 127.15 (2016), pp. 6000 –6006. ISSN: 0030-4026. DOI: 10.1016/j.ijleo.2016.04.019.

[47] Zhong Long et al. "Study on the electronic structure of α-U2N3 by {XPS} and first principles". In: *Journal of Alloys and Compounds* 664 (2016), pp. 745 –749. ISSN: 0925-8388. DOI: 10.1016/j.jallcom.2016.01.013.

[48] N. Pauly, F. Yubero, and S. Tougaard. "Quantitative analysis of satellite structures in {XPS} spectra of gold and silver". In: *Applied Surface Science* 383 (2016), pp. 317 –323. ISSN: 0169-4332. DOI: 10.1016/j.apsusc.2016.03.185.

[49] Walter T. Ralston et al. "Soft X-ray spectroscopy studies of adsorption and reaction of {CO} in the presence of {H2} over 6 nm MnO nanoparticles supported on mesoporous Co3O4". In: *Surface Science* 648 (2016). Special issue dedicated to Gabor Somorjai's 80th birthday, pp. 14 –22. ISSN: 0039-6028. DOI: 10.1016/j.susc.2015.12.006.

Books

[50] E.E. Koch. *Basic principles and applications of EXAFS*. Handbook on Synchrotron Radiation v. 1b,pt. 10. North Holland Pub. Co., 1983. ISBN: 9780444864253. URL: https://books.google.no/books?id=EsnvAAAAMAAJ.

[51] Jens Als-Nielsen and Des McMorrow. *Elements of modern x-ray physics*. New York, NY: Wiley, 2001. URL: https://cds.cern.ch/record/479075.

[52] Matthew Newville. *Fundamentals of XAFS*. Reviews in Mineralogy and Geochemistry vol. 78 no. 1 33-74. Mineralogical Society of America, 2014. DOI: 10.2138/rmg.2014.78.2. URL: http://dx.doi.org/10.2138/rmg.2014.78.2.

Software

For the accomplishment of the work a numerous list of software products and search engines was used and listed as follows:

- Google Chrome, used for web-browsing and page searching, https://www.google.com/chrome
- LaTeX, scientific typesetting system, integrated with several external packages, https://www.ctan.org/;
- Share Latex, a browser LaTeXcompiler, https://www.sharelatex.com
- Mathematica, used for analytical and mathematical evaluations, www.wolfram.com/mathematica
- Athena, XAFS data processing software part of the Demeter Package for XAFS data processing and analysis, http://bruceravel.github.io/demeter/
- MatLab, used for plots and to support Mathematica, http://se.mathworks.com/products/matlab/
- Gimp, for image editing, https://www.gimp.org/

Report type-setted in LaTeX, from original source, with ShareLatex compiler. Structure adapted from a template by Marvin Rausand RAMS-NTNU.

Universitet i Stavanger, Norway, 14 June 2016

■